Single-Cell Transcriptomic Landscape Deciphers Intratumoral Heterogeneity and Subtypes of Acral and Mucosal Melanomas

Yunyan Li[1,2], Ziyang Cui[3], Xiaole Song[4,5], Yeqing Chen[6], Cang Li[1,2], Junfeng Shi[4], Wenkang Qian[7], Guoxin Ren[8], Jiang Zhou[1,2], Chunpu Li[1,2], Xiaoqing Ma[1,2], Yifan Chen[1,2], Dongdong Jia[7], Yongli Zhang[9], Zhilin Zhang[1,2], Ronghao Zhang[1,2], Zhaotian Zhang[1,2], Yong Chen[10,11], Zhixiang Xu[12], Wantao Chen[8], Xiao Miao[13], Hongmeng Yu[4,14], Jianxin Chen[9], Kai Wang[15], Colin R. Goding[16], Zhi Wei[6], Tao Li[7], and Rutao Cui[1,2]

ABSTRACT

Purpose: To identify the specific intratumoral and microenvironmental heterogeneity of acral melanoma (AM) and mucosal melanoma (MM), we aimed to delineate their distinct cellular compositions, evolutionary trajectories, and subtype-specific therapeutic strategies.

Experimental Design: Single-cell transcriptomic and genomic landscapes were analyzed across 42 melanoma (28 AM, 11 MM, and 3 nonacral cutaneous melanoma) samples, supplemented by *in vitro* and *in vivo* validation. Tumor and stromal cells were profiled using single-cell RNA sequencing, whole-exome sequencing, and functional assays, including transwell migration, co-culture systems, and xenograft models.

Results: Tumor cells exhibited divergent evolutionary routes, with MM dominated by MGP^+/$PCOLCE^+$ subpopulations showing high epithelial-to-mesenchymal transition potential. MM displayed elevated neutrophil infiltration and $CXCL3^+$ tumor-associated macrophages, whereas AM was enriched with $PI16^+$ cancer-associated fibroblasts promoting tumor proliferation. Molecular classification revealed MM subtypes: an antigen-presenting subtype linked to favorable outcomes and a proliferative subtype associated with recurrence. $TIGIT^+$ regulatory T cells were enriched in AM, suggesting targeted inhibition potential. Genomic analysis connected BRAF/NRAS mutations to $ALDOA^+$ stem-like tumor cells and identified prostaglandin D2 synthetase as a therapeutic target in triple–wild-type/melanomas.

Conclusions: Our study provides a comprehensive comparison of AM and MM, uncovering subtype-specific stromal–immune interactions and molecular programs. The findings highlight actionable targets (e.g., TIGIT in AM and $CXCL3^+$ macrophages in MM) and propose a framework for precision therapies, biomarker-driven trials, and risk stratification to improve outcomes in these aggressive melanomas.

Introduction

Over recent years, it has become clear that beyond the initial mutations responsible for cancer initiation, disease progression is largely driven by bidirectional interactions between phenotypically plastic cancer cells and the microenvironment (1). Moreover, specific phenotypic states may be associated with differentiation, proliferation, or invasion and some exhibit tolerance to targeted therapies or immunotherapies. Understanding the repertoire of phenotypes present within cancers and their interactions with the stromal cells that shape the microenvironment is therefore a key issue.

Melanoma represents an excellent model for understanding how microenvironment–cancer cell interactions generate substantial phenotypic diversity and therapy resistance (2). However, most research on melanoma has focused on the cutaneous form of the disease that is driven by UV exposure with activation of the *BRAF* or *NRAS* oncogenes with at least six different phenotypic states being identified to date (3).Yet, although cutaneous melanoma (CM) has been a key focus, melanomas also occur in other anatomic locations with different driver mutations and in which UV irradiation is not a cause. However, although genetic drivers have been identified for non-CMs, including acral melanoma (AM) and mucosal melanoma (MM; 4), much less is known about the tumor microenvironment, the degree of phenotypic heterogeneity, and the complex interactions between the stroma and plastic melanoma cells.

MM is a rare form of melanoma that develops in mucous membranes with more aggressive features. The 5-year survival of MM,

[1]Skin Disease Research Institute, The Second Affiliated Hospital, Zhejiang University School of Medicine, Hangzhou, China. [2]Cancer Institute (Key Laboratory of Cancer Prevention and Intervention, China National Ministry of Education), Zhejiang Provincial Clinical Research Center for CANCER, Cancer Center of Zhejiang University, The Second Affiliated Hospital, Zhejiang University School of Medicine, Hangzhou, China. [3]Department of Dermatology and Venereology, Peking University First Hospital, Peking University, Beijing, China. [4]ENT institute and Department of Otorhinolaryngology, Eye & ENT Hospital, Fudan University, Shanghai, China. [5]Mucosal Melanoma Diagnosis and Treatment Center, Eye & ENT Hospital, Fudan University, Shanghai, China. [6]Department of Computer Science, Ying Wu College of Computing, New Jersey Institute of Technology, Newark, New Jersey. [7]Zhejiang Cancer Hospital, Hangzhou Institute of Medicine (HIM), Chinese Academy of Sciences, Hangzhou, Zhejiang. [8]Shanghai Key Laboratory of Stomatology & Shanghai Research Institute of Stomatology, National Clinical Research Center of Stomatology, Ninth People's Hospital, School of Medicine, Shanghai Jiao Tong University, Shanghai, China. [9]School of Life Science, Beijing University of Chinese Medicine, Beijing, China. [10]Department of Oncology, Shanghai Medical College, Fudan University, Shanghai, China. [11]Department of Musculoskeletal Oncology, Fudan University Shanghai Cancer Center, Shanghai, China. [12]School of Life Sciences, Henan University, Kaifeng, China. [13]Department of Dermatology, Shuguang Hospital of Traditional Chinese Medicine, Shanghai University of Traditional Chinese Medicine, Shanghai, China.

Translational Relevance

Our study delineates the distinct intratumoral and microenvironmental heterogeneity of acral melanoma (AM) and mucosal melanoma (MM), identifying subtype-specific therapeutic vulnerabilities. The dominance of MGP^+/$PCOLCE^+$ tumor cells with high epithelial-to-mesenchymal transition potential in MM and $PI16^+$ cancer-associated fibroblasts in AM highlights actionable targets for precision therapies. Molecular classification of MM into antigen-presenting and proliferative subtypes, linked to clinical outcomes, offers a framework for tailored immunotherapy and risk stratification. Enhanced neutrophil and $CXCL3^+$ macrophage interactions in MM suggest strategies to mitigate immunosuppression, whereas elevated *TIGIT* in AM regulatory T cells supports targeted inhibition. These insights enable the development of subtype-specific regimens, biomarker-driven trials, and combination therapies to improve survival in these aggressive melanomas.

considering all stages at the time of diagnosis, is 14% compared with 80% for CM (5, 6). The most common driver *BRAF* mutations found in CM are usually rare in MM (7). *BRAF* mutations were only identified in 26% of AM and 4% to 6% of MM in comparison with 50% to 80% in nonacral CM (8). Patients with MM are therefore insensitive to BRAF/MEK-targeted inhibition (9). By contrast, a few unique mutations were identified in MM, such as *SF3B1* R625 codon mutations (10). Although MM showed a favorable response to checkpoint inhibitions, such as anti–PD-1 antibodies, anti-CTLA4 antibodies, or both combination immunotherapy, the response rates remain much lower than those in CM (11).

AM is characterized by a highly immunosuppressive microenvironment (12–15). The "cold" tumor microenvironment includes the depletion of cytotoxic $CD8^+$ T cells, enrichment of regulatory T cells (Treg), the presence of exhausted $CD8^+$ T cells, and the reduced presence of other immune cells, such as NK and γδ T cells, when compared with CM (14). One most recent study indicates that an early and monoclonal seeding pattern in vertical invasion is from AM to invasive AM, and that $APOE^+CD163^+$ macrophages promote tumor epithelial-to-mesenchymal transition (EMT) via IGF1–IGF1R interaction, displaying one mechanism of the immunosuppressive microenvironment inducing metastasis (16). Collectively, these studies indicate that there is a significant heterogeneity between the tumor cells and immune microenvironment in different subtypes of melanoma. Analyzing the heterogeneity of tumor cells and immune microenvironment among different subtypes of melanoma will help elucidate the differences in therapeutic targets and immunotherapeutic effects among different subtypes of melanoma. Although relevant studies have found heterogeneity between tumor cells and the immune microenvironment in melanoma of the skin and AM (11, 12), the heterogeneous cellular composition in the microenvironment of MM remains unclear. The underlying connection between single-cell transcriptome of melanoma and specific gene mutations has not been reported. Moreover, a molecular clarification of MM is also required for the precision medicine of patients diagnosed with this disease.

Materials and Methods

Patient specimens

For the single-cell RNA sequencing (scRNA-seq) analysis, 14 patients diagnosed with AM and 11 patients diagnosed with MM who underwent curative surgical resection were included. Fourteen patients diagnosed with AM were sourced from the Zhejiang Cancer Hospital. Eleven patients diagnosed with MM were sourced from Fudan University (ENT Hospital), Shanghai Ninth People's Hospital, and Fudan University Shanghai Cancer Center. The remaining 17 patients' datasets were obtained from the GEO database under accession numbers GSE215120 and GSE189889. These include 10 AM, 4 AM-Met (acral melanoma–metastasis), and 3 CM samples. Then, we used the 23 CM samples from EGA: EGAD00001009291 to validate our conclusions (17). Detailed clinicopathologic characteristics of these patients are summarized in Supplementary Table S1. Tumor cells in both primary and metastatic lesions were confirmed by pathologists via cytological detection during surgery and examination of paraffin sections after surgery. The primary lesions of these patients had received targeted therapy, immunotherapy, or other antitumor therapies prior to surgery. All clinical specimens in this study were collected with informed consent for research use and were approved by the institutional review boards of Zhejiang Cancer Hospital; Department of Otorhinolaryngology, Eye & ENT Hospital; Shanghai Ninth People's Hospital; and Fudan University Shanghai Cancer Center in accordance with the Declaration of Helsinki, under protocol

[14]Research Unit of New Technologies of Endoscopic Surgery In Skull Base Tumor(2018RU003), Chinese Academy of Medical Sciences, Beijing, China. [15]Department of Respiratory and Critical Care Medicine, Center for Oncology Medicine, the Fourth Affiliated Hospital of School of Medicine, and International School of Medicine, International Institutes of Medicine, Zhejiang University, Yiwu, China. [16]Ludwig Institute for Cancer Research, Nuffield Department of Clinical Medicine, University of Oxford, Oxford, United Kingdom.

Y. Li, Z. Cui, X. Song, Y. Chen, and C. Li contributed equally to this article.

Corresponding Authors: Rutao Cui, The Second Affiliated Hospital, Zhejiang University School of Medicine, Jiefang Road, Hangzhou, Zhejiang Province, 310053, China. E-mail: rutaocui@zju.edu.cn; Cang Li, The Second Affiliated Hospital, Zhejiang University School of Medicine, Jiefang Road, Hangzhou, Zhejiang Province, 310053, China. E-mail: licang@zju.edu.cn; Zhi Wei, Department of Computer Science, Ying Wu College of Computing, New Jersey Institute of Technology, 218 Central Avenue, Newark, NJ, 07102. E-mail: zhiwei@njit.edu; Colin R. Goding, Ludwig Institute for Cancer Research, Nuffield Department of Clinical Medicine, University of Oxford, Roosevelt Drive, Headington, Oxford, OX3 7DQ, UK. E-mail: colin.goding@ludwig.ox.ac.uk; Kai Wang, the Fourth Affiliated Hospital of School of Medicine, and International School of Medicine, Zhejiang University, Shangcheng Avenue, Yiwu, Zhejiang Province, 322000, China. E-mail: kaiw@zju.edu.cn; Tao Li, Zhejiang Cancer Hospital, East Banshan Road, Hangzhou, Zhejiang Province, 310022, China. E-mail: litao@zjcc.org.cn; Jianxin Chen, School of Life Science, Beijing University of Chinese Medicine, East Third Ring North Road, Beijing, 100029, China. E-mail: cjx@bucm.edu.cn; Hongmeng Yu, Eye & ENT Hospital, Fudan University, Fenyang Road, Shanghai, 200031, China. E-mail: hongmengyush@163.com; and Xiao Miao, Shuguang Hospital of Traditional Chinese Medicine, Puan Road, Shanghai 200437, China. E-mail: 0000002623@shutcm.edu.cn

Clin Cancer Res 2025;31:2495–514

doi: 10.1158/1078-0432.CCR-24-3164

numbers IRB202307, IRB20231127, IRB2021061, IRB1903198-8, and IRB2018-86-T77. Consent was obtained for the publication of relevant clinical information that may potentially identify individuals, including details such as age, gender, therapy, overall survival time, clinical stage, etc. Written informed consent was also obtained from all patients participating in this study for the use of their tissue samples and clinical information.

Preparation of single-cell suspensions

The fresh tissue was initially transferred to a petri dish and was carefully placed on ice to maintain a controlled temperature. It was then gently washed with the 1× PBS solution to effectively remove any blood stains, grease, or other adherents from its surface. Subsequently, the tissue was meticulously cut into small pieces, each approximately 0.5 mm^2 in size. All washed fragments were added into a dissociation solvent containing 0.35% collagenase IV, 5.2 mg/mL papain, and 120 U/mL DNase I. The mixture was placed in a water bath and agitated at 100 rpm for 20 minutes at 37°C to facilitate tissue dissociation. To terminate the dissociation process, PBS containing 10% FBS was used. Next, the cell suspension was filtered through a 70- to 30-μm cell strainer to remove any debris or large particles. The suspension was then centrifuged at 4°C at 300*g* for 5 minutes to collect the cell sediment. After centrifugation, the cell sediment was carefully collected and resuspended in 100 μL of 1× PBS (0.04% BSA) solution. To eliminate red blood cells from the suspension, 1 mL of 1× red blood cell lysis buffer (MACS 130-094-183, 10×) was added, and the mixture was allowed to react at room temperature or on wet ice for 2 to 10 minutes. These cells were then centrifuged 300*g* for 5 minutes again at 4°C to collect cell sediment. To further purify the cell suspension, 100 μL of cell removal beads (MACS 130-090-101) was added, and the mixture was thoroughly mixed and incubated at room temperature for 15 minutes. At the end of the incubation period, the binding buffer was added, and the suspension was passed through mass spectrometry columns (130-042-201) to remove any reagents and dead cells removal beads. The cells were then centrifuged once again at 4°C at 300*g* for 5 minutes to collect the cell sediment. The cell sediment was resuspended in 1× PBS (0.04% BSA) and centrifuged again at 4°C at 300*g* for 5 minutes. This washing step was repeated twice to ensure the removal of any remaining contaminants. Following the tissue dissociation, red blood cell lysis, and dead cell removal steps, the candidate cells were obtained. A cell suspension was then formed by adding 100 μL of 1× PBS (0.04% BSA) into the purified cells. To assess cell viability, the trypan blue staining method was used. Finally, the number of cells was counted using the Countess II automated cell counter. Samples with a total cell number <200,000 and a nuclear ratio <80% were discarded.

Chromium 10× Genomics library and sequencing

Using the 10× Genomics Chromium Single-Cell 3′ Kit (v3), the single-cell suspension was loaded into the 10× Chromium chip, with the aim of capturing 8,000 cells. Following the generation of Gel bead-in-EMulsion and barcoding, the Gel bead-in-EMulsion reverse transcription reaction was conducted to obtain cDNAs. The cDNAs were then amplified using PCR. After amplification, the cDNAs were fragmented, end-repaired, A-tailed, ligated to an index adapter, and further amplified. The library was sequenced by LC-Bio Technologies on the Illumina NovaSeq 6000 sequencing system (RRID: SCR_016387), using paired-end sequencing with a read length of 150 bp, ensuring a minimum of 20,000 reads per cell.

scRNA-seq data processing

The Cell Ranger pipeline (version 7.1.0; RRID: SCR_017344) was used for demultiplexing, barcode processing, alignment, and initial clustering of the raw scRNA-seq profiles. The raw sequencing reads were mapped, annotated, and quantified using the GRCh38 reference annotation file (accessible at https://cf.10xgenomics.com/supp/cell-exp/refdata-gex-GRCh38-2020-A.tar.gz). The unique molecular identifier (UMI) count matrix was processed using Seurat in the R package (version 5.0.3; RRID: SCR_016341; ref. 18), and a consistent standard was applied to filter cells with UMI/gene numbers falling outside the range of the mean value ± 2 times the median absolute deviation, assuming a Gaussian distribution of UMI/gene numbers for each cell. After a visual inspection of the cell distribution, additional low-quality cells were discarded, specifically those in which more than 25% of the counts were attributed to mitochondrial genes. Additionally, the DoubletFinder package (version 2.0.2; RRID: SCR_018771) was used to identify potential doublets. We treated individual samples as distinct batches and used the Harmony algorithm (RRID: SCR_022206; ref. 19) with the default sigma and theta parameters to correct for batch effects. Following the application of these quality control criteria, a total of 319,382 high-quality single cells were retained for downstream analysis. Normalized expression profiles of all samples were merged using the Merge() function in R (version 4.3.0). Subsequently, library size normalization, log-transformation, and identifying the 3,000 most highly variable genes were performed using the SCTransform() function in Seurat.

Principal components were computed on the basis of expression profiles of the top 3,000 highly variable genes. The FindNeighbors() and FindClusters() functions in Seurat were used for cell clustering. The RunUMAP() function was used for visualization when appropriate. Cells were visualized using a two-dimensional Uniform Manifold Approximation and Projection (UMAP) algorithm, implemented through the RunUMAP() and DimPlot() functions. Marker genes in each cluster were identified using the FindAllMarker() function in Seurat. Specifically, for a given cluster, the FindAllMarkers() function identified positive markers compared with all remaining clusters.

Whole-exome sequencing

Whole-exome sequencing (WES) was performed on frozen tissues obtained from 12 patients diagnosed with melanoma. DNA extraction was carried out using the QIAGEN DNeasy Blood & Tissue Kit or the QIAamp DNA FFPE Tissue Kit (both from QIAGEN). Subsequently, the DNA was fragmented using the M220 Focused-ultrasonicator (Covaris) and subjected to sequencing library construction. Exome capture was performed using the Twist Exome 2.0 Plus kit (Twist Bioscience) according to the manufacturer's recommended protocol. The final libraries were sequenced for paired-end 150-bp reads using the Illumina NovaSeq 6000 sequencing system (Illumina) at LC-Bio Technologies.

WES data processing

Prior to alignment, the low-quality reads—(i) reads containing sequencing adapters and (ii) nucleotide with q quality score <20—were removed by using fastp (20). For the alignment step, Burrows–Wheeler Aligner (RRID: SCR_010910; ref. 21) was utilized to perform reference genome (hg19) alignment with the reads contained in paired FASTQ files. In the first postalignment processing step, Picard tools (http://broadinstitute.github.io/picard/; RRID: SCR_006525) were used to identify and mark duplicate reads from BAM files. In the second postalignment processing step, local read

realignment was performed to correct the potential alignment errors around indels. Local realignment was performed to determine if a site should be realigned. A computationally intensive algorithm was applied to determine the most consistent placement of the reads with respect to the indel and remove misalignment artifacts. Each base of each read has an associated quality score, corresponding to the probability of a sequencing error. Due to the systematic biases, the reported quality scores are known to be inaccurate and should be recalibrated prior to genotyping. After recalibration, the recalibrated quality score in the output BAM more closely corresponded to the probability of a sequencing error. Variant calls can be generated using either the HaplotypeCaller or UnifiedGenotyper tools in GATK v3.5 (https://gatk.broadinstitute.org; RRID: SCR_001876). Both methods analyze evidence of variation from the reference genome through Bayesian inference. A Gaussian mixture model is fit to assign the accurate confidence score to each putative mutation call and evaluate new potential variants. Biological functional annotation is a crucial step in finding the links between genetic variation and disease. Variant effect predictor (RRID: SCR_007931; ref. 22) was used to add biological information to a set of variants. Due to the unavailability of blood samples, we lacked matched normal samples for the tumors. To reliably identify somatic mutations, we used a pan-cancer panel of normal established by LC-Bio Technologies as the negative control for all samples in the GATK Mutect2 pipeline.

Cells were labeled on the basis of the mutation results of WES of each patient, such as triple–wild-type (triple-WT), BRAF, NRAS, and NF1, and then analyzed for proportion differences in each subpopulation in the tumor.

Single-cell deep constrained clustering

Single-cell deep constrained clustering (scDCC) is a deep learning model (23) designed to produce biologically interpretable clustering based on established domain knowledge. We applied scDCC to our integrated single-cell dataset after batch effect removal using Harmony (19). The input to scDCC comprised the expression matrix of the top 3,000 most highly variable genes identified with the SCTransform method (24) in Seurat (18), along with cell constraint pairs indicating which cells should be assigned to different clusters. To generate the rationale constraint pairs, we calculated the enrichment scores for major cell types using AUCell (RRID: SCR_021327; ref. 25). The detailed marker gene list fed to AUCell is demonstrated in Supplementary Table S2. We selected the top 100 cells with the highest scores in each category as representatives and created cannot-link constraint pairs between these representative cells from different cell types. After the training step, we extracted the 32-dimensional embedding layer and applied UMAP for further dimensionality reduction and visualization. scDCC effectively used consistent biological knowledge, achieving superior performance compared with Seurat's purely unsupervised clustering.

Definition of cell scores and signatures

The average expression [measured by $\log_2$ (CPM + 1), where CPM denotes counts per million] of four cytotoxicity-associated genes (*TNF*, *IFNG*, *GZMA*, and *GZMK*) and eight exhausted markers (*PDCD1*/*PD-1*, *TOX*, *CTLA4*, *HAVCR2*/*TIM-3*, *HAVCR1*, *LAG3*, and *BTLA*) was used to define the cytotoxic, the exhausted score of $CD4^+$ and $CD8^+$ T cells. To score macrophages, the gene sets reported (26) were applied to calculate the M1/M2 polarization scores (Supplementary Table S4).

Trajectory and RNA velocity analysis

To perform cell trajectory inference, the Monocle2 (27) package (version 2.30.0; RRID: SCR_016339) and Monocle3 (28) package (version 1.3.6; RRID: SCR_018685) were used, respectively. The counts from the Seurat object were extracted, and then CytoTRACE 2 (bioRxiv 2024.03.19.585637) was used to compute the potency score of each cell and assess the state of cell differentiation. These potency scores back to the Seurat object were mapped to create a boxplot based on clusters/subclusters. The clusters/subclusters with the highest potency scores were defined as the initial point of pseudotime. Initially, the raw count data were converted from the Seurat object to the CellDataSet object using the ImportCDS() function in Monocle. Subsequently, the DifferentialGeneTest() function was used to select ordered genes (with a q value < 0.01) that were deemed likely to be informative for ordering cells along the pseudotime trajectory. After this, dimensional reduction clustering analysis was conducted using the reduceDimension() function. This was then followed by trajectory inference using the orderCells() function with default parameters. To track changes in gene expression over time, the plot_genes_in_pseudotime() function was used. In order to recover the cellular dynamics of the indicated cells, velocyto.py was used to extract splicing information from the *.bam files generated by Cell Ranger. The calculation of RNA velocity values for each gene in each cell and the embedding of the RNA velocity vector in low-dimensional space were carried out using the R package velocyto.R (version 0.6). Finally, the velocity fields were projected onto the UMAP embedding obtained using Seurat.

Nonnegative matrix factorization

To classify the molecular subtypes of tumor cells, we used the GeneNMF package (version 0.4.0). Initially, we applied nonnegative matrix factorization (NMF; RRID: SCR_023124) to a list of Seurat objects in order to extract gene programs. The selection of $k = 3$ for the number of meta-programs (MP) was determined through iterative experimentation. Specifically, we observed that each melanoma type (CM, AM, and MM) exhibited two major MPs along with an additional, smaller MP containing features of intermediate characteristics. This choice of $k = 3$ balanced the need to capture key biological features while maintaining clinical relevance for our objective to explore the relationship between MPs and clinical outcomes. Subsequently, we clustered the gene programs derived from all melanoma samples and grouped them into MPs. Lastly, we computed MP metrics and identified the most influential genes within each MP ($k = 3$; nfeature = 50).

Copy-number variation

Single-cell copy-number variation (CNV) evaluation was conducted for each cell on the chromosome using the R package inferCNV (version 1.18.1; RRID: SCR_021140). The CNV score for each cell was calculated as the column mean of SDs of gene expression values from 1, which was then converted into a data frame. Specifically, the CNV score (CNV_score) was computed as the mean of $(\text{expression} - 1)^2$ across all genes for each cell. Subsequently, genes were arranged on the basis of their chromosomal positions, and a moving average of gene expression was calculated using a sliding window encompassing 101 genes. To normalize the expression data, the mean value was subtracted, centering the expression levels around zero. The inferCNV analysis was performed with the "denoise" option enabled, using default settings for the hidden Markov model and setting the "cutoff" parameter to 0.1.

K-nearest neighbors

The K-nearest neighbor algorithm was used to classify the sample point by calculating the distance between it and known sample points and then using a majority voting method, using the R package FNN (version 1.1.4) with k set to 21.

Differential expression and pathway analysis

To identify differentially expressed genes, we used the FindMarkers() function with the test.use parameter set to "presto" in the Seurat package. In order to estimate pathway activities in individual cells, we applied the gene set variation analysis (GSVA) using the standard settings implemented in the GSVA package (version 1.50.1; RRID: SCR_021058; ref. 29). For loading the gene set file, we used the GSEABase package (version 1.64.0) and msigdbr package (version 7.5.1; RRID: SCR_022870). This gene set file was downloaded from the Kyoto Encyclopedia of Genes and Genomes database (accessible at https://www.kegg.jp/) and msigdbr (accessible at https://www.gsea-msigdb.org/gsea/msigdb). Subsequently, differences in pathway activities scored in each cell were calculated using the limma package (version 3.58.1).

Cell–cell interaction analysis

We used CellPhoneDB (RRID: SCR_017054; ref. 30) and CellChat (RRID: SCR_021946; ref. 31) to infer unbiased cell–cell interactions between melanoma cells and microenvironmental cells (myeloid/T/B cells and fibroblasts), respectively. The normalized gene expression data were used as the input of CellPhoneDB. CellPhoneDB infers the potential interaction strength between two cell clusters based on the gene expression levels of ligand–receptor (LR) pairs while considering the structural composition of both ligands and receptors. The potential interaction strength between the two cell subsets was estimated on the basis of the expression of their respective LR pairs. The enriched LR interactions were calculated using the permutation tests with 1,000 iterations. Interactions with P values <0.05 were considered statistically significant. Based on the number of significant pairs, interactions that were highly specific among cell types were then prioritized.

Correlation to public datasets

Bulk RNA-seq data and clinical data of melanoma samples were obtained from The Cancer Genome Atlas–SKCM (RRID: SCR_003193; ref. 32). In the expression matrix, genes with low expression levels were filtered out, retaining only those genes with expression levels >0 in more than half of the samples. Subsequently, the expression data were normalized using the CPM function from the edgeR package (33) and then subjected to logarithmic transformation using $\log_2$. For the MGP^+MEL (S5) subgroups in our integrated scRNA-seq, genes with avg_$\log_2$FC > 0.55 and adjusted $P < 0.01$ compared with the rest of the melanoma cells were defined as MGP^+MEL signature (Supplementary Table S3). The GSVA package was used to calculate the enrichment score for each patient, and then the patients were divided into high-score ($n = 222$) and low-score ($n = 223$) groups based on the median score. The Kaplan–Meier (KM) survival method, implemented via the R package survival (version 3.5.7; RRID: SCR_021137), was used to analyze the prognosis between these groups, with differences in survival curves assessed using the log-rank test.

Public scRNA-seq datasets for AM were collected from Zhang and colleagues (12) and Li and colleagues (14), and datasets for CM were collected from Pozniak and colleagues (17).

Cell line and cell culture

A375 (CC-Y1030; RRID: CVCL_0132), A875 (CC-Y1037; RRID: CVCL_4733), HEK293T (CC-Y1010; RRID: CVCL_0063), B16 (CC-Y2013; RRID: CVCL_F936), MEWO (JCM-H1419; RRID: CVCL_0445), and NHDF (BNCC358600) cells were purchased from EK-Bioscience company, BeNa Culture Collection, and Jiesimo company. A375, A875, and HEK293T were cultured in complete DMEM (C11995500CP, Gibco) supplemented with 10% FBS (10091148, Gibco) and 100 U/mL penicillin–streptomycin. MEWO cells were cultured in complete minimum essential medium (10% bovine serum and 100 U/mL penicillin–streptomycin). B16 cells were cultured in complete RPMI 1640 medium (C11875522CP, Gibco; 10% bovine serum and 100 U/mL penicillin–streptomycin).

Plasmids and short hairpin RNA

All transient overexpression plasmids, as well as overexpression plasmids of lentivirus and short hairpin RNA plasmids, used in this study were constructed by OBiO Technology Corp., Ltd (Shanghai), and validated by sequencing. The short hairpin RNA sequence of aldolase A (*ALDOA*) and prostaglandin D2 synthetase (*PTGDS*) was 5′-GAGGGCCTATTTCCCATGA-3′ and 5′-GACTTGTATTGTTATTTAA-3′.

Stable gene silencing and overexpression in cells

Simply put, HEK293T cells were transfected with 1.5 μg of lentiviral plasmid, 1 μg psPAX2, and 0.5 μg pMD2.G in a six-well plate. Cells were infected with lentivirus for 24 hours, incubated in fresh culture medium, and then selected using 2 μg/mL puromycin.

Cell counting and colony formation assay

Fibroblasts with overexpressing *PI16* and tumor cells (1×10^3) were transferred at a 1:10 ratio into 96-well plates. The growth of the cells was determined by using Cell Counting Kit-8 (CCK-8; C0038, Beyotime). After 48 hours, CCK-8 solution (10 μL) was added to each well, and the cells were incubated for an additional 1 hour. Then, the value of each well was measured by a microplate reader at 450 nm.

For colony formation assay, cells (0.5×10^3) were seeded in six-well plates and cultured in the incubator supplied with 5% CO_2 at 37°C. When the cells were prepared, they were washed with PBS and then stained using crystal violet (Sigma-Aldrich) for 20 minutes at room temperature. Colonies were counted using ImageJ. All the experiments were repeated three times.

Transwell migration and invasion assays

Transwell migration and invasion assays were conducted using 24-well Transwell permeable inserts (Corning, #3422). For the invasion assay, Transwell chambers were precoated with Matrigel matrix (Corning, #354234). MGP and PCOLCE overexpression plasmids (2 μg each) were transfected into A375 and A875 cells by using Lipofectamine 3000 Transfection Reagent (L3000015, Thermo Fisher Scientific) in a six-well plate and cultured for 24 hours. Approximately 20,000 cells of different groups were starved for 24 hours, then diluted in 200 μL of serum-free medium and then seeded into the upper chambers. In the lower chambers, 600 μL of medium containing 10% FBS was added. After 48 hours of incubation, chambers were removed, and the cells in the upper chamber were wiped off. Cells on the lower membrane surface were fixed with methanol for 10 minutes and then stained using 0.5% crystal violet solution

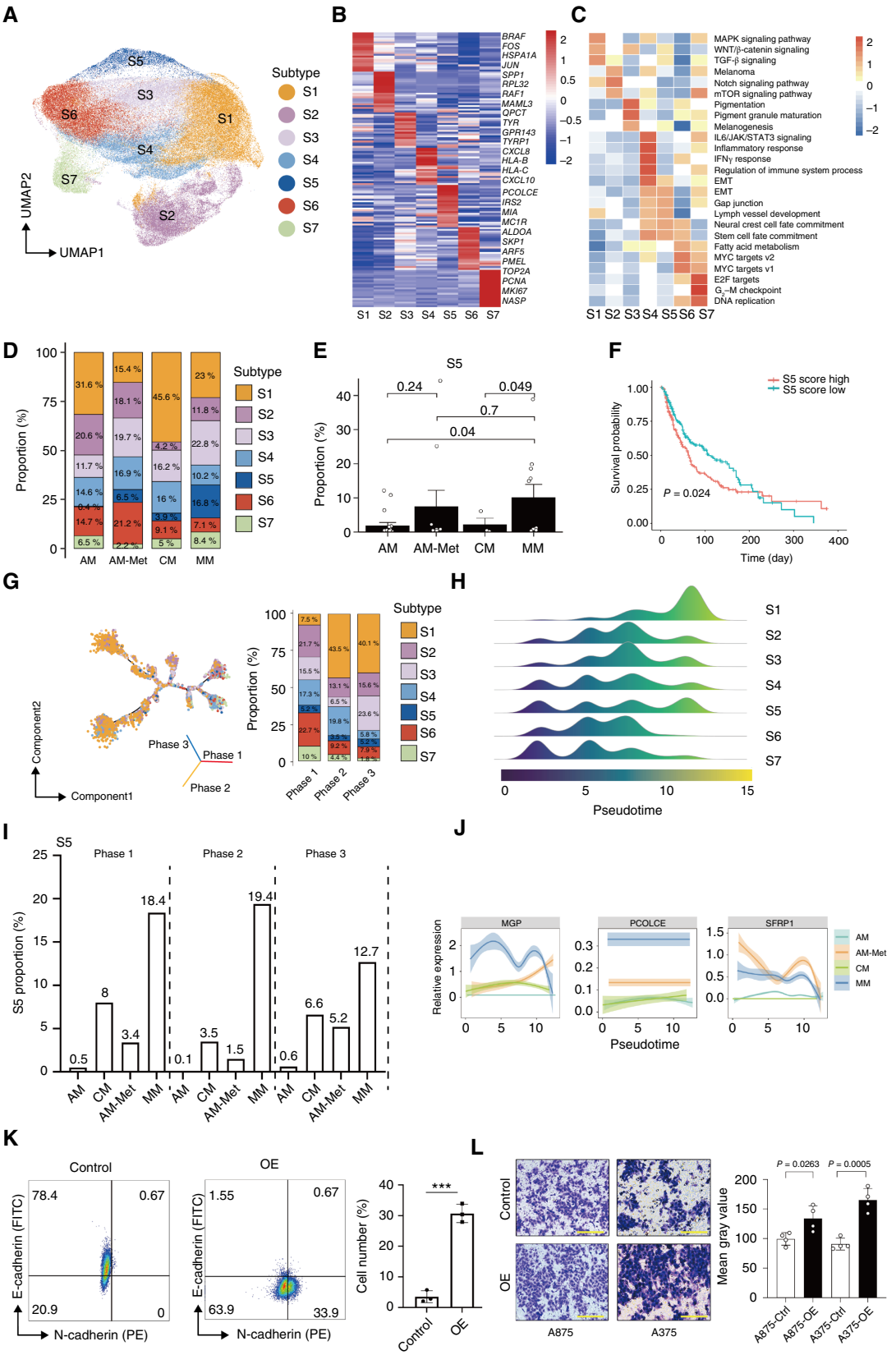
A
S5
S3
S6
S1
S4
S7
S2
UMAP2
UMAP1
Subtype
S1
S2
S3
S4
S5
S6
S7
B
BRAF
FOS
HSPA1A
JUN
SPP1
RPL32
RAF1
MAML3
QPCT
TYR
GPR143
TYRP1
CXCL8
HLA-B
HLA-C
CXCL10
PCOLCE
IRS2
MIA
MC1R
ALDOA
SKP1
ARF5
PMEL
TOP2A
PCNA
MKI67
NASP
S1 S2 S3 S4 S5 S6 S7
C
MAPK signaling pathway
WNT/β-catenin signaling
TGF-β signaling
Melanoma
Notch signaling pathway
mTOR signaling pathway
Pigmentation
Pigment granule maturation
Melanogenesis
IL6/JAK/STAT3 signaling
Inflammatory response
IFNγ response
Regulation of immune system process
EMT
EMT
Gap junction
Lymph vessel development
Neural crest cell fate commitment
Stem cell fate commitment
Fatty acid metabolism
MYC targets v2
MYC targets v1
E2F targets
G2–M checkpoint
DNA replication
S1 S2 S3 S4 S5 S6 S7
D
Proportion (%)
AM
AM-Met
CM
MM
Subtype
S1
S2
S3
S4
S5
S6
S7
E
S5
Proportion (%)
0.24
0.049
0.7
0.04
AM
AM-Met
CM
MM
F
S5 score high
S5 score low
Survival probability
P = 0.024
Time (day)
G
Component2
Component1
Phase 3
Phase 1
Phase 2
Proportion (%)
Subtype
S1
S2
S3
S4
S5
S6
S7
H
S1
S2
S3
S4
S5
S6
S7
Pseudotime
I
S5
Phase 1
Phase 2
Phase 3
S5 proportion (%)
0.5
8
3.4
18.4
0.1
3.5
1.5
19.4
0.6
6.6
5.2
12.7
AM
CM
AM-Met
MM
J
MGP
PCOLCE
SFRP1
Relative expression
Pseudotime
AM
AM-Met
CM
MM
K
Control
OE
78.4
0.67
20.9
0
1.55
0.67
63.9
33.9
E-cadherin (FITC)
N-cadherin (PE)
Cell number (%)
***
Control
OE
L
Control
OE
A875
A375
P = 0.0263
P = 0.0005
Mean gray value
A875-Ctrl
A875-OE
A375-Ctrl
A375-OE

(Beyotime) for 20 minutes. Migrating and invading cells were visualized and counted using a Nikon inverted microscope.

Flow cytometry

After overexpressing *MGP* and *PCOLCE* in six-well plates and culturing for 24 hours, the cells were collected and fixed with 2% paraformaldehyde solution. The fixed cells were labeled with antibodies against CD45 (BioLegend, #368516), E-cadherin (BD Pharmingen, #560062), and N-cadherin (BD Pharmingen, #562119) and used to detect tumor cell invasion status by using flow cytometry.

Peripheral blood samples (20 mL) were collected from patients with AM and CM for flow cytometry. For assessing the CTLA4 and TIGIT expression levels in Tregs of AM and CM, staining was performed using antibodies against CD45 (BioLegend, #368516), CD4 (Abcam, #ab213215), FOXP3 (Abcam, #ab215206), CTLA4 (Abcam, #ab237712), and TIGIT (Abcam, #ab321793). The flow cytometry data were analyzed using FlowJo v10.8.1.

Immunoblot analysis

Cell lysis buffer (RIPA, 89901, Thermo Fisher Scientific) was used to extract total cellular protein. All antibodies used are shown in Supplementary Material (Supplementary Table S7).

Melanoma xenograft mice

Cells with gene overexpression or knockout (1.5×10^5) were mixed with 100 μL of culture medium supplemented with 10% basement membrane matrix (Corning, #354234), and then subcutaneously injected into the axilla of 8- to 10-week-old nude mice (purchased from Shanghai Model Organisms Center, Inc.). Tumor size was measured once in 3 days. Mice were euthanized when the allowed endpoint was reached. All mice were kept in pathogen-free conditions in the animal facilities of the Experimental Animal Center at Zhejiang University of Traditional Chinese Medicine. All animal experiments were reviewed and approved by the Second Affiliated Hospital of Zhejiang University School of Medicine and the Experimental Animal Center of Zhejiang University of Traditional Chinese Medicine.

Multiplex immunofluorescence staining

In brief, different melanoma tissue sections were serially stained by using the AlphaTSA Multiplex IHC Kit (AXT36100031, AlphaX). A total of six antibodies were used, including myeloperoxidase (Abcam, #AB208670, RRID: AB_2864724), CD4 (MXB Biotechnologies, #RMA-0620, RRID: AB_2925216), FOXP3 (Cell Signaling Technology, #98377, RRID: AB_2747370), PMEL (Thermo Fisher Scientific, #MA1-34759, RRID: AB_1955861), VIM (Abcam, #ab92547, RRID: AB_10562134), and PI16 (Proteintech, #12267-1-AP, RRID: AB_10697651). Fluorescent images were collected using the THUNDER–DM6B fluorescence microscope and analyzed using ImageJ. For **Figs. 2F**, **4I**, and **5F**, counts were based on a representative field of view. For **Fig. 3H**, counts were based on the average gray value within a representative field of view.

Co-culture experiment of neutrophil and melanoma cells

Neutrophil isolation was performed using density gradient centrifugation. The blood of participants with MM and AM (Mel26, Mel27, and Mel12 in Supplementary Table S1) was collected by venipuncture into lithium heparin–coated vacutainers. According to the manufacturer's instructions, the neutrophils were isolated by single-step centrifugation of whole blood onto Polymorphprep (Axis Shield). Briefly, collected blood was layered onto Polymorphprep and centrifuged at 500*g* for 40 minutes. The granulocyte layer was carefully removed and resuspended in RPMI 1640 media (Gibco) with added 25 mmol/L HEPES (Gibco). Erythrocytes were removed by hypotonic lysis and platelets removed by further centrifugation of the cells at 150*g* for 3 minutes. In the end, neutrophils were resuspended in RPMI 1640 media. A cell counter was used to count the concentration.

For isolation of $CD8^+$ T cells, the peripheral blood (20 mL) was collected from patients with melanoma Mel34. Single-cell suspension was added to the $CD8^+$ immunomagnetic bead solution (Miltenyi Biotec) and incubated for 30 minutes at 4°C. After being washed two times with buffer, the $CD8^+$ T cells were collected through the mass spectrometry column in the magnetic field. The number of $CD8^+$ T cells was counted by using a cell counter.

Cell co-culture validation was conducted using 24-well Transwell permeable inserts (Corning, #3422). About 5,000 neutrophil cells were diluted in 300 μL of medium (supplemented with 10% FBS) and seeded into the upper chambers. In the lower chambers, co-culture of $CD8^+$ T cells with melanoma tumor cells (1.5×10^5) at a ratio of 1:5 was supplemented in media with 10% FBS and cocultured at 37°C in 5% CO_2. After 24 hours of incubation, the upper chambers were removed. Cells on the lower chambers were washed with PBS. Subsequently, the cells were digested using trypsin, and the number of melanoma cells was counted using a cell counter.

Co-culture experiment of cancer-associated fibroblast and melanoma cells

The fibroblasts are derived from NHDF (human origin) and fibroblasts extracted from C57BL (mouse origin). Cell co-culture validation was conducted using 24-well Transwell permeable inserts (Corning, #3422). Melanoma cells (A875 or B16) were placed in the lower chamber of a 24-well plate, either with fibroblasts overexpressing PI16 or with primary fibroblasts, for 48 hours. Cells on the lower chambers were fixed with methanol for 10 minutes and stained using 0.5% crystal violet solution (Beyotime) for 20 minutes. After multiple washes with PBS, all cells were eluted with anhydrous ethanol and the optical density at 570 nm was measured.

Figure 1.

MM is dominated by MGP^+ and $PCOLCE^+$ S5 cells. **A,** Seven annotated melanoma molecular subtypes were classified by UMAP plot in AM, AM-Met, CM, and MM. **B,** Cluster-specific gene heatmap of each subtype. **C,** GSVA of these subtypes. **D,** Bar plot showing the population distribution of each subtype in AM, AM-Met, CM, and MM. **E,** Histogram illustrating the distribution of S5 subtype in AM, AM-Met, CM, and MM. The two-sided unpaired Student *t* test was used to identify significant difference. Error bars represent the mean ± SEM. **F,** KM overall survival curves comparing patients with high S5 scores ($n = 222$) with those with low S5 scores ($n = 223$). **G,** Pseudotime-ordered analysis (left) of these cell subtypes. Three cell fates were identified. Bar plot (right) showing the populations of each subtype in the different branches of the trajectory. **H,** Ridge plots displaying the dynamic changes in cell number along the pseudotime. **I,** Bar plot showing the proportions of S5 in the different branches of the trajectory. **J**, Two-dimensional plots showing the dynamic expression levels of MGP, PCOLCE, and SFRP1 genes over pseudotime in AM, AM-Met, CM, and MM. **K,** Flow cytometry plots showing EMT tumor cells from the control (Ctrl) and MGP overexpression (OE) cell line ($n = 3$). The bar plot displays EMT tumor cell proportions. Student *t* test. **L,** Transwell plot of MGP OE in A875 and A375 cell lines (left). The bar plot displays migrated tumor cell number (right).

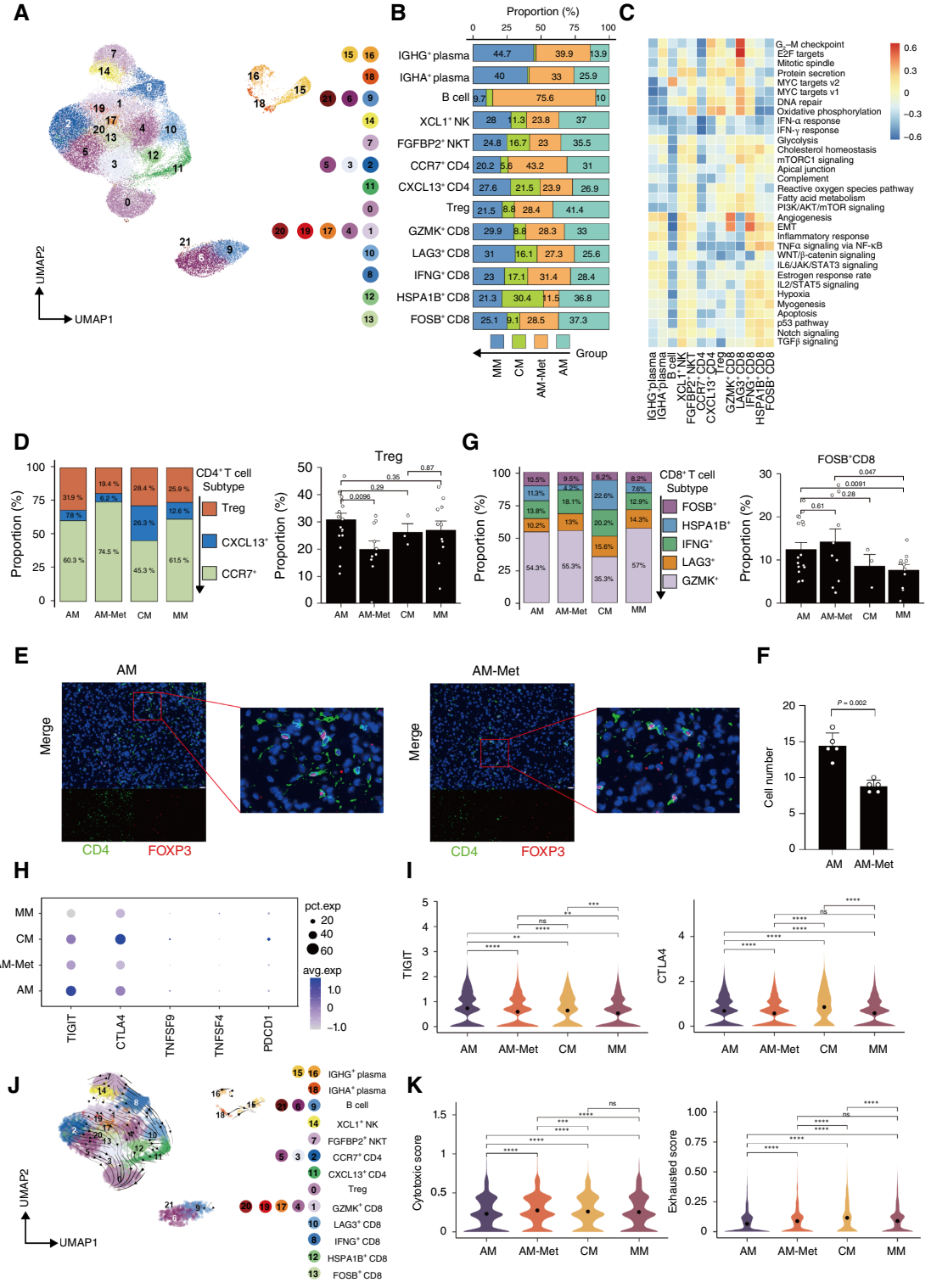

Figure 2.

TIGIT is a suitable inhibitor for AM. **A,** UMAP plot illustrating tumor-infiltrating lymphocytes (TIL) in AM, AM-Met, CM, and MM. Color coding by TIL subclusters. **B,** Bar plot displaying the population distribution of indicated subclusters in AM, AM-Met, CM, and MM. **C,** GSVA of selected hallmark pathways in these subclusters. **D,** Bar plot displaying the population distribution of indicated $CD4^+$ T-cell subclusters (left) in AM, AM-Met, CM, and MM. Histogram (right) illustrating the percentage of subtype of T cells across these groups. The two-sided unpaired Student *t* test was used to identify the significant difference. Error bars represent the mean ± SEM. **E** and **F,** Representative IF images (**E**) and quantification (**F**) of $FOXP3^+CD4^+$ Tregs in AM and AM-Met. (*Continued on the following page.*)

Statistical analysis and study design

The unpaired, two-tailed *t* test comparisons were performed between two groups in xenograft studies. The KM survival method was used to analyze the prognosis. The differences in survival curves were assessed by using the log-rank test. The statistical tests were performed with biological replicates. $P < 0.05$ was considered statistically significant. *, $P < 0.05$; **, $P < 0.01$; and ***, $P < 0.001$.

Data availability

The raw sequence data reported in this article have been deposited in the Genome Sequence Archive (Genomics, Proteomics & Bioinformatics) and OMIX in National Genomics Data Center, China National Center for Bioinformation/Beijing Institute of Genomics, Chinese Academy of Sciences under https://ngdc.cncb.ac.cn/gsa-human/browse/HRA010364 and https://ngdc.cncb.ac.cn/omix/release/OMIX009050. The raw sequencing data are available for noncommercial purposes under controlled access due to data privacy laws, accessible through formal request to the corresponding authors. Code used in this article is deposited at https://github.com/lobotyy/Melanoma-scRNA. For public datasets analysis, Li and colleagues' dataset was retrieved from GSE189889; Zhang and colleagues' dataset was retrieved from GSE215120; and Pozniak and colleagues' dataset was retrieved from EGAD00001009291. The remaining data are available within the article, Supplementary Information. The raw data behind all of the figures and supplementary figures are available upon request.

Results

Diverse composition and evolutionary routes of AM and MM

To interrogate the tumor heterogeneity of anatomically distinct melanoma subtypes, single-cell transcriptomic and genomic landscapes were analyzed in AM ($n = 28$), MM ($n = 11$), and nonacral CM ($n = 3$; Supplementary Table S1). A total of 319,382 cells were obtained. A total of eight broad cell types, including endothelial cells, melanoma cells, cancer-associated fibroblasts (CAF), myeloid cells, T/NK cells, B cells, plasma cells, and epithelial cells were identified using scDCC and marker genes as listed in Supplementary Figs. S1 and S2 (34).

To decipher the landscape of tumor cells, based on unsupervised cell clustering analysis, we grouped 113,115 melanoma tumor cells into seven main subgroups (**Fig. 1A**). These subgroups exhibited distinct functional gene expression signatures (**Fig. 1B**) and Gene Ontology. All subgroups were characterized by their distinct functional signatures as demonstrated in **Fig. 1C**. Subgroup 5 (S5), with a high expression of *MGP* and *PCOLCE*, was specifically enriched with the expression of genes linked to EMT (**Fig. 1C**; Supplementary Fig. S3D). Notably, different melanoma samples exhibited significantly different proportions of each subgroup, respectively (Supplementary Fig. S3A–S3C). Statistical analysis revealed that MM had a significantly higher proportion of the EMT-enriched S5 subgroup than AM and CM (**Fig. 1D** and **E**; Supplementary Fig. S3E and S3F). To characterize the S5 identified in MM, it may be interesting to explore its behavior in other melanoma types. Therefore, we analyzed data from The Cancer Genome Atlas to determine whether the S5 signature is associated with poorer overall survival in CMs. We found that patients with high S5 scores tended to exhibit worse prognosis initially (<200 days) but showed better outcomes in the longer term (>250 days; **Fig. 1F**; Supplementary Table S3). These results indicate that the S5 subgroup is a characteristic subgroup of MM.

Next, we applied the cell trajectory analysis through Monocle2 to capture the trajectory of tumor evolution and defined the evolution stages as phases I to III (**Fig. 1G** and **H**). The proportions of the subcluster pseudotime trajectory varied significantly among the AM, AM-Met, CM, and MM (Supplementary Fig. S4A and S4B). Phase I contained a substantial proportion of S6 (22%) and S7 (10%) cells, and the proportions of S6 and S7 decreased with increasing differentiation (from phase I to phase III), indicating their potential role as early or progenitor-like states within this phase. The overexpressing high expression of proliferation-related genes such as *MKI67* and *TOP2A* and tumor stem cell markers like *VIM* and *MIA* were identified in phase I (**Fig. 1G**; Supplementary Fig. S4C and S4D). S6 cells have high proliferation and metastasis potential as stem-like cells (Supplementary Fig. S4E–S4G). A tiny proportion of S1 was identified in phase I. The proportion of S1 was increased at the later stages, especially in phase II. The overexpression of immune-related genes including *SPP1*, *HLA-C*, and *STAT3* was identified in phase I (Supplementary Fig. S4C). Phase II was primarily composed of S5, characterized by a significant EMT signature (**Fig. 1G**). The evolutionary characteristics indicated that S6 and S7 cells may represent early or progenitor-like states in the melanoma cell trajectory, although the directionality of this trajectory in cancer remains complex and may not directly reflect developmental processes (Supplementary Fig. S4E and S4F). When compared with other subtypes, AM-Met mainly originated from S6 and has only a minimal proportion of S7.

Interestingly, unlike other types of melanoma, the proportion of S5 was found to be similar across different phases in some patients with MM (five of 11), despite the fact that S5 was present at a higher proportion specifically in these five patients (**Fig. 1I**). This result indicates a potential competing advantage of S5 in these patients with MM. Correspondingly, several marker genes, including *MGP* and *PCOLCE*, were found to highly express in S5. The overexpression of *MGP* and *PCOLCE* genes was observed throughout the entire evolutionary trajectory in five of 11 patients with MM (**Fig. 1J**; Supplementary Table S10).

To determine whether *MGP* and *PCOLCE* contribute to driving the phenotype of S5, we evaluated the cellular invasive ability by examining the expression of N-cadherin and E-cadherin after the overexpression of *MGP* and *PCOLCE* in melanoma cells. Previous studies have demonstrated that the downregulation of E-cadherin and overexpression of N-cadherin are hallmark characteristics of EMT (35). Flow cytometry results indicated that cells overexpressing *MGP*

(*Continued*.) Quantification was based on a representative field of view. Scale bar, 50 μm. *P* value = 0.002; the assay was triplicated. The two-sided unpaired Student *t* test was used to identify the significant difference. Error bars represent the mean ± SD. **G,** Bar plot displaying the population distribution of indicated $CD8^+$ T cells (left) in AM, AM-Met, CM, and MM. Histogram (right) illustrating the percentage of $FOSB^+$ T cells in different types of melanoma. The two-sided unpaired Student *t* test was used to identify the significant difference. Error bars represent the mean ± SEM. **H,** Dot plot showing percent expression (pct.exp) and average expression (avg.exp) of TIGIT, CTLA4, TNFSF9, TNFSF4, and PDCD1 in AM, AM-Met, CM, and MM, respectively. **I,** Violin plots displaying the average expression of TIGIT and CTLA4 in the Tregs of AM, AM-Met, CM, and MM. ****, $P < 0.0001$; Kruskal–Wallis rank-sum test was used. **J,** RNA velocity analysis demonstrating the evolutionary trajectory of immunity cell subclusters. **K,** Violin plots displaying the cytotoxic scores (right) and exhausted scores (left) in AM, AM-Met, CM, and MM. ****, $P < 0.0001$; the Kruskal–Wallis rank-sum test was used.

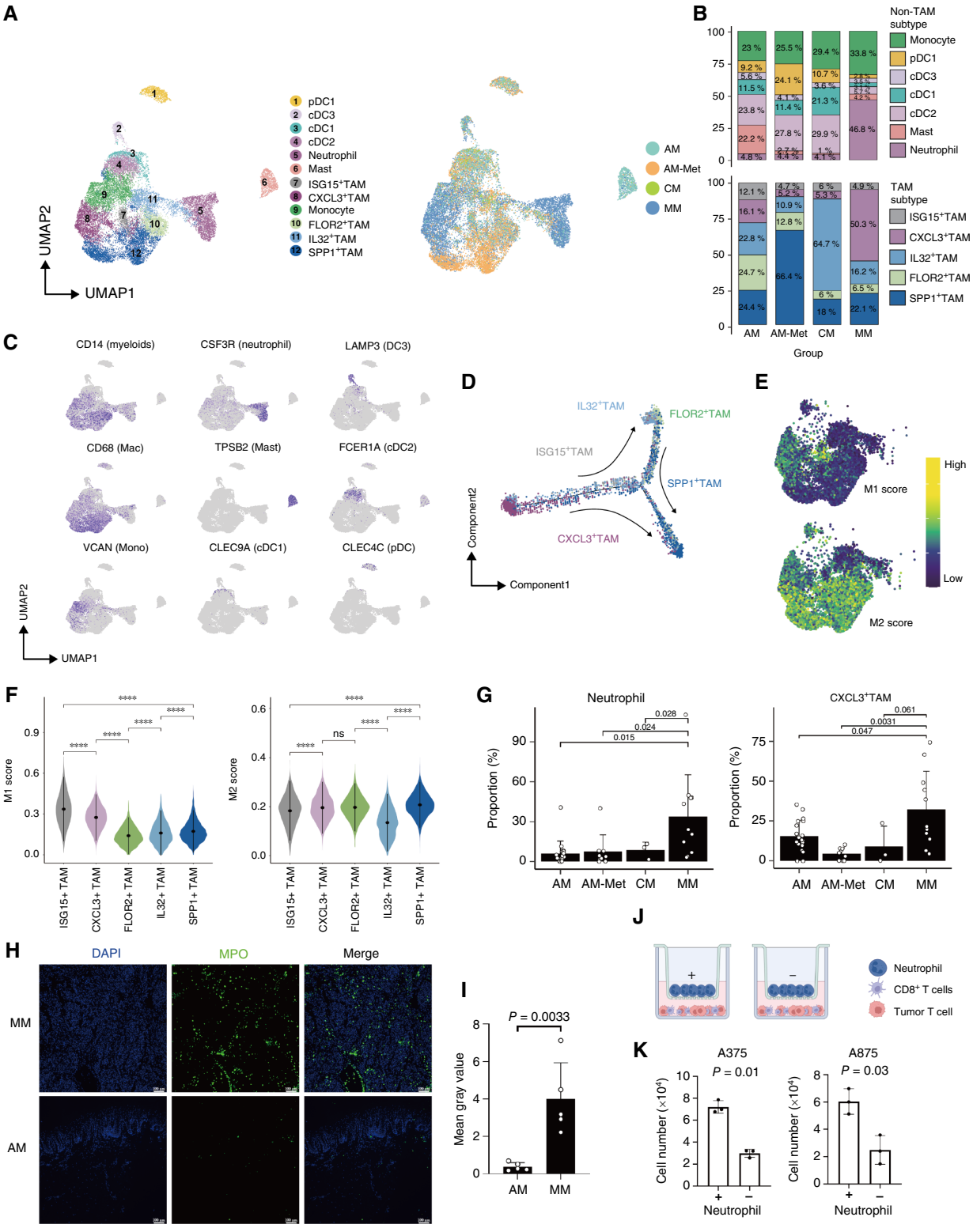

Figure 3.

Stronger infiltration of neutrophils and CXCL3$^+$ tumor-associated macrophages in MM. **A,** UMAP plot of tumor-infiltrating myeloid cells (left) and their distribution (right) in AM, AM-Met, CM, and MM. **B,** Bar plot displaying the population distribution of specific subclusters within non-TAMs and TAMs across the AM, AM-Met, CM, and MM groups. **C,** Feature plots of classical marker genes for subcluster annotation. DC, dendritic cell; Mac, macrophage; (*Continued on the following page.*)

or *PCOLCE* induced the downregulation of E-cadherin and overexpression of N-cadherin (**Fig. 1K**). These results indicate that EMT was activated after *MGP* or *PCOLCE* overexpression. Further exploration of tumor invasiveness through transwell assay revealed that overexpression of *MGP* and *PCOLCE* enhanced tumor invasiveness (**Fig. 1L**; Supplementary Fig. S4H). All these results indicate that the overexpression of *MGP* and *PCOLCE* contributes to the invasiveness activity of S5 cells.

Analysis of lymphocytes in AM and MM

A total of 63,455 lymphoid cells were extracted, grouped into 21 clusters, and subsequently identified as 13 subclusters based on marker genes listed in reference (36). Initially, we classified these lymphocytes into B cells, NK cells, and T cells based on marker gene expression. T cells were further subdivided and categorized into $CD4^+$ T cells and $CD8^+$ T cells. Within these groups, distinct subpopulations were identified. These include plasma cells ($IGHG^+$ and $IGHA^+$), $CD4^+$ T cells [$CCR7^+$ (naïve), $CXCL13^+$ (exhausted), and $FOXP3^+$ (Treg)], and $CD8^+$ T cells [$GZMK^+$ (effector), $FOSB^+$ (memory), $HSPA1B^+$ (memory), $IFNG^+$ (cytotoxic), and $LAG3^+$ (exhausted); **Fig. 2A**]. The proportions of these subclusters varied significantly among patients and in between the AM, AM-Met, CM, and MM groups (**Fig. 2B**; Supplementary Fig. S5A–S5D). The GSVA of hallmark pathways revealed *IL2/STAT5* signaling enrichment in $CD8^+$ T-cell subclusters in all different types of melanomas (**Fig. 2C**; Supplementary Fig. S5E). The proportion of Tregs within $CD4^+$ T cells was found to be significantly higher in AM than in AM-Met, but not in CM and MM (**Fig. 2D**). We also found that MM exhibited a similar T-cell immune landscape with AM and CM. There were fewer $FOSB^+$ $CD8^+$ T cells in MM. However, the number of cytotoxic CD8 cells was still no different (**Fig. 2G**; Supplementary Fig. S5F). Interestingly, the overexpression of inhibitory genes, such as *TIGIT* and *CTLA4*, was identified in Tregs compared with T cells and NK cells (Supplementary Fig. S5G and S5H). We also found that *CTLA4* expression was significantly higher in Tregs of CM than in Tregs of AM and MM (**Fig. 2H** and **I**; Supplementary Fig. S6C–S6E). Anti-CTLA4 antibodies have been used in melanoma treatment clinically and are usually more efficient in patients with CM than in those with AM (37). Our results indicate that the lower response rate of anti-CTLA4 antibodies in AM and MM may correlate with the lower expression of *CTLA4* in Tregs of AM and MM. Notably, we also found that the expression of *TIGIT*, one of the most promising targets of immunotherapy (38) of Tregs, was significantly higher in AM than in CM and MM. The lowest expression of *TIGIT* in Tregs was found in MM (**Fig. 2H** and **I**; Supplementary Fig. S6C and S6D). On the basis of all these results of *TIGIT*, we speculate that the response rate of anti-TIGIT antibody therapies should be lower in patients with MM than in patients with AM and CM. RNA velocity analysis indicated that T cells originated from naïve cells and then differentiated into memory, effector, and cytotoxic cells, ultimately culminating into exhaustion (**Fig. 2J**; Supplementary Fig. S6F and S6G). Additionally, we measured cytotoxic scores and exhausted scores of $CD8^+$ T cells (39) and found that the exhausted scores of $CD8^+$ T cells were significantly higher in CM than in AM and MM (**Fig. 2K**; Supplementary Fig. S5H and S5I). This result is consistent with the better immunotherapy response rate in CM than in AM and MM (40). We also found MM bore higher cytotoxic scores and lower exhausted scores than CM (**Fig. 2K**).

To preliminarily verify the scRNA-seq result of lymphocytes, multiplex immunofluorescence (IF) staining was performed. The staining results confirmed that $FOXP3^+$ Tregs were indeed more prevalent in AM than in AM-Met (**Fig. 2E** and **F**; Supplementary Fig. S6A and S6B). Peripheral blood samples were collected from patients with three AMs and three CMs for flow cytometry. Flow cytometry analysis also showed that the proportion of $TIGIT^+FOXP3^+$ $CD4^+$ T cells in AM is significantly higher than that in CM (Supplementary Fig. S6E). Taken together, these results indicate that the differences in the immune microenvironment of different subtypes of melanoma may be key influencing factors to influence the effectiveness of immunotherapy across different forms of melanoma.

Higher neutrophils and $CXCL3^+$ tumor-associated macrophages are identified in MM

Twelve clusters of myeloid cells were identified from 21,662 isolated myeloid cells, including dendritic cells, neutrophils, mast cells, monocytes, and tumor-associated macrophages (TAM; **Fig. 3A**). The proportions of these subclusters varied significantly among patients (Supplementary Fig. S7A and S7B). TAMs were further classified into five subgroups based on specific marker genes (41), including $ISG15^+$, $CXCL3^+$, $FLOR2^+$, $IL32^+$, and $SPP1^+$ TAMs (**Fig. 3B** and **C**; Supplementary Fig. S7C). Monocle2 analysis indicated that the pseudotime trajectory began at $ISG15^+$ TAMs; progressed to be $CXCL3^+$, $FLOR2^+$, and $IL32^+$ TAMs; and ultimately culminated in becoming $SPP1^+$ TAMs (**Fig. 3D**; Supplementary Fig. S7D and S7E). The high expression of most chemokines and cytokine molecules was identified in $CXCL3^+$ TAMs, including *CXCL2* and *CXCL3* (Supplementary Fig. S7F). M1/M2 polarization scores (26) indicated that most macrophages were skewed toward the M2 phenotype in the AM ecosystem. Specifically, low M1/M2 scores were identified in $IL32^+$ TAM cells. $ISG15^+$ and $CXCL3^+$ TAM cells showed higher M1 scores (**Fig. 3E** and **F**). Furthermore, the higher infiltration of $CXCL3^+$ TAMs was found in MM than in AM and CM (**Fig. 3G**; Supplementary Fig. S7G). Considering that *CXCL3* is the main chemotactic factor of neutrophil recruitment (42), we subsequently detected neutrophils in MM and found that, consistent with $CXCL3^+$ TAMs, MM exhibited a higher infiltration of neutrophils than AM and CM. This result is consistent with the higher infiltration of $CXCL3^+$ TAMs in MM (**Fig. 3G**; Supplementary Fig. S7H).

To preliminarily verify the scRNA-seq results of neutrophils in MM, IF staining of myeloperoxidase was performed. The high

(*Continued.*) Mono, monocyte. **D,** Pseudotime-ordered analysis of TAM subclusters. Arrows indicate the potential evolutionary direction in the trajectory. **E,** Feature plots showing the M1/M2 polarization signatures in TAMs. **F,** Violin plots illustrating the M1/M2 polarization signatures in the indicated TAM subclusters. Significance was determined using the Kruskal–Wallis rank-sum test. ****, $P < 0.0001$; ns, $P > 0.05$. **G,** Bar plot displaying the population distribution of indicated neutrophil (denominator is non-TAM) and $CXCL3^+$ TAM (denominator is TAM) in AM, AM-Met, CM, and MM. The two-sided unpaired Student *t* test was used to identify the significant difference. Error bars represent the mean ± SEM. **H** and **I,** Representative IF image (**H**) and quantification (**I**) of MPO^+ cells in formalin-fixed, paraffin-embedded tissues of MM and AM. MPO positive indicates neutrophil cells. Cells were stained with anti-MPO (green) and DAPI (4',6-diamidino-2-phenylindole; blue). Quantification was based on the average gray value within a representative field of view. Scale bar, 100 μm. $P = 0.0033$; the two-sided unpaired Student *t* test was used to identify the significant difference. Error bars represent the mean ± SD. **J** and **K,** Co-culture system of neutrophil, $CD8^+$ T cells, and tumor cell line (A375 and A875). **J,** The bar plot shows the count of melanoma cells. **K,** Three repeated experiments; the two-sided unpaired Student *t* test was used to identify the significant difference. Error bars represent the mean ± SD. DC, dendritic cells. [**J**, Created in BioRender. Li, Y. (2025), https://BioRender.com/d18n133.]

prevalence of neutrophils was identified in MM (**Fig. 3H** and **I**). Besides their intrinsic killing function, neutrophils also exhibit immunosuppressive effects in tumors (43). We speculate that a high proportion of neutrophils in MM promote immune evasion by inhibiting immune cells ($CD8^+$ T cells) in melanoma. To verify this hypothesis, we extracted neutrophils and $CD8^+$ T cells from the blood of patients with melanoma and then co-cultured these with melanoma cells (A375 and A875) to detect the changes of T-cell killing ability (**Fig. 3J**). $CD8^+$ T cells were directly co-cultured with melanoma cells in the lower chamber, whereas neutrophils were located in the upper chamber. The co-culture studies revealed that neutrophils inhibit T-cell killing ability in melanoma (**Fig. 3K**). This result indicated the immunosuppression role of neutrophils in MM. The high inflation of neutrophils in MM may correlate with the low immunotherapy response of MM.

$PI16^+$ CAFs were characterized in stromal cells of AM

To decipher the landscape of CAFs in AM and MM, seven clusters of CAFs were identified from 21,346 isolated fibroblasts, including $IL6^+$ CAFs, $PTGDS^+$ CAFs, muscle cells, $CD53^+$ CAFs, $POSTN^+$ CAFs, $APOD^+$ CAFs, and $PI16^+$ CAFs (**Fig. 4A**; Supplementary Fig. S8A). The proportions of these subclusters varied significantly among patients and in between AM, AM-Met, CM, and MM (Supplementary Fig. S8B and S8C). The identified subgroups were characterized by distinct marker genes as listed in **Fig. 4B** (44, 45). We observed a significant heterogeneity in the proportions of CAFs in AM, AM-Met, CM, and MM. $PI16^+$ CAFs were significantly more prevalent in AM and AM-Met than they were in CM and MM (**Fig. 4C** and **D**; Supplementary Fig. S8D). These CAF clusters were characterized by distinct signaling pathways and metabolic features. Specifically, the enrichment of inflammatory response pathways, *IL2/STAT5* signaling, and cholesterol homeostasis was identified in $PTGDS^+$, $IL6^+$, and $POSTN^+$ CAF cells (**Fig. 4E**). The elevated fatty acid metabolism and oxidative phosphorylation were identified in $PI16^+$ and $APOD^+$ CAF cells. Monocle3 and CytoTRACE studies indicated that the pseudotime trajectory began at $PI16^+$ CAFs; progressed to become $APOD^+$, $POSTN^+$, and $PTGDS^+$ CAFs; and ended as $IL6^+$ CAFs and $CD53^+$ CAFs (**Fig. 4F**; Supplementary Fig. S8E). This is consistent with previous reports that $PI16^+$ CAFs are the initial subpopulation with the potential to differentiate into other CAF subtypes (45).

To validate the results collected from the single-cell sequencing, we used multiplex IF staining to identify whether $PI16^+$ CAFs were more prevalent in AM than in MM. Our staining results confirmed the results collected from scRNA-seq (**Fig. 4G** and **H**). Given the role of fibroblasts in tumor proliferation (46), we further performed the co-culture between PI16-overexpressing fibroblasts and tumor cells to identify whether $PI16^+$ CAFs directly control tumor

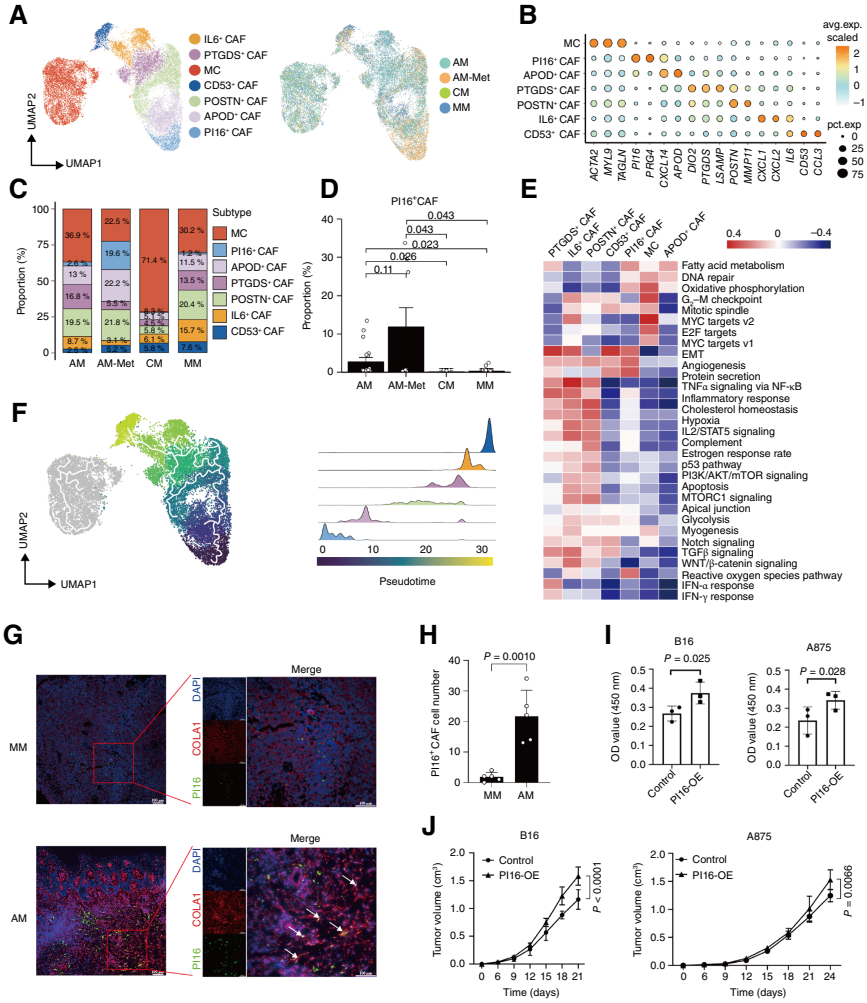

Figure 4.
$PI16^+$ CAF is more abundant in AM and AM-Met than in CM and MM. **A,** UMAP plot of CAFs (left) and their distribution (right) in AM, AM-Met, CM, and MM. **B,** Dot plot showing the percentage expression (pct.exp) and average expression (avg.exp) level of marker genes in these subclusters. **C,** Bar plot displaying the population distribution of indicated subclusters in AM, AM-Met, CM, and MM. **D,** Histogram illustrating the populations of neutrophils in AM, AM-Met, CM, and MM. The two-sided unpaired Student *t* test was used to identify significant difference. Error bars represent mean ± SEM. **E,** GSVA of selected hallmark pathways in these subclusters. **F,** Visualization of the cell embedding landscape inferred by Monocle3 (left). Subtypes are labeled by colors (right). **G** and **H,** Representative IF images (**G**) and quantification (**H**) of $PI16^+VIM^+$ CAFs in fixed, paraffin-embedded tissues of MM and AM. Cells were stained with anti-COLA1 (red), anti-PI16 (green), and DAPI (4',6-diamidino-2-phenylindole; blue). Quantification was based on a representative field of view. Scale bar, 100 μm. $P = 0.0010$; the two-sided unpaired Student *t* test was used to identify the significant difference. Error bars represent the mean ± SEM. **I,** Co-culture system of $PI16^+$CAF and melanoma cells. The bar plot shows the OD (optical density) value of the CKK-8 trial (down). The Student *t* test was used to identify significant difference. **J,** Growth curve for xenograft experiments with indicated tumor cells mixed with PI16 overexpression in fibroblasts inoculated subcutaneously into the flanks of nude mice (A875) and C57BL mice (B16). Visible tumors were measured every 3 days. Data are mean ± SEM relative to the control group ($n = 5$).

proliferation. As a control, we used fibroblasts that do not have PI16 overexpression. Our results indicated that PI16$^+$ fibroblasts directly regulate tumor proliferation (**Fig. 4I**). Furthermore, we validated the effect of PI16$^+$ fibroblasts on tumor growth in nude mice. Immunodeficient mice were grafted with co-cultured PI16-overexpressing fibroblasts and B16 or A875 melanoma cells. Xenograft weight and survival assay indicate that injection of PI16-overexpressing fibroblasts significantly induced tumor growth and progression (**Fig. 4J**; Supplementary Fig. S8F and S8G). These results suggest that PI16$^+$ CAFs promote the proliferation of melanoma cells.

Distinct cellular interactome landscape of AM and MM

To identify the cross-talk between tumor cells and other components in the tumor microenvironment in AM and MM, CellPhoneDB and CellChat were used to analyze intercellular LR interactions (**Fig. 5A**; Supplementary Fig. S9A–S9C). Generally, the interactions among CAFs were significantly higher than in other cell types in all melanoma (**Fig. 5A**; Supplementary Fig. S9C). Notably, we found that the interaction number and strength were slightly higher in the ecosystem of AM-Met than of AM and MM (Supplementary Fig. S9B). Comparing the levels of cellular interactions across different melanoma subtypes, the higher interactions were detected in MM, wherein strong interactions between melanoma cells and stromal cells were observed (**Fig. 5A**). For LR interactions, 67 LR pairs specific to individual melanoma subtypes were identified, including 18 pairs in MM (**Fig. 5B**). Specifically, more than half (10/18) of the MM-specific LR pairs are related to the CXCL3$^+$ TAMs in which upregulated *DLL4* and *NOTCH2* signals were detected (**Fig. 5B**). These results suggest a critical role of CXCL3$^+$ TAMs in regulating immunity response and tumor growth in MM. Similarly, neutrophils were also highly enriched in many MM-specific LR pairs, such as *CXCL6* and *CXCR1* (**Fig. 5B**). Moreover, PI16$^+$ CAFs, which are crucial in AM (**Fig. 4G** and **H**), were found to be correlated with more than half of the AM-specific LR pairs (**Fig. 5C**). Among them, we noticed that the interactions between PI16$^+$ CAFs and melanoma cells were significantly higher in AM than in CM and AM-Met (**Fig. 5B**). The Kyoto Encyclopedia of Genes and Genomes pathway analysis indicates that *PI3K*/*AKT* signaling in tumor cells was the major signaling pathway after LR interactions of PI16$^+$ CAFs and melanoma cells in AM (**Fig. 5D**). Consistently, the AM-specific RSPO1–LGR4 interaction was highly enriched in PI16$^+$ CAFs in AM. This interaction activates WNT signaling to eventually activate PI3K/AKT signaling (**Fig. 5B**).

To validate the results collected from the single-cell sequencing, we used multiplex IF staining and confirmed that overlapping of PI16$^+$ CAFs with melanoma cells was more prevalent in AM than in MM (**Fig. 5E** and **F**).

The single-cell transcriptomic landscape connects with the specific genomic landscape

To further interrogate the tumor heterogeneity of AM and MM, the genomic landscape of AM and MM was identified by WES (**Fig. 6A**; Supplementary Fig. S10A and S10B; Supplementary Table S9). The sequencing samples included the melanoma samples that we collected ($n = 12$) and the published sequencing results ($n = 28$; refs. 12, 14). Different driver mutations were identified in our melanoma samples, including *BRAF* and *NRAS* mutations (**Fig. 6A**). Correlating these mutations with single-cell sequencing data revealed a significant increase in the S6 subgroup in melanoma with *NRAS* or *BRAF* mutation compared with melanoma with the wild-type of *BRAF*, *NRAS*, and *NF1* (triple-WT) mutations, which are defined as stem-like subtypes characterized with a high expression of *ALDOA* and *ARF5* (**Fig. 6B** and **C**; Supplementary Fig. S10C).

Next, we conducted expression analysis of genes involved in melanoma with different mutations or triple-WT. In triple-WT melanoma, high reactive oxygen species production and protein transportation were detected in the S6 subgroup. However, the enriched ribosome pathways and metabolism-related pathways including oxidative phosphorylation and glycolysis/gluconeogenesis were detected in the S6 of melanoma with different driver mutations like *BRAF*, *NRAS*, and *NF1* (**Fig. 6D**). The MAPK signaling pathway was found to be downregulated in melanoma with *BRAF* mutations (Supplementary Fig. S10D). Furthermore, we conducted expression analysis of genes involved in different mutation types and triple-WTs. We found the expression of multiple glycolysis/gluconeogenesis genes, including *ALDOA*, were elevated in *BRAF* mutation (**Fig. 6E**). *ALDOA* is a key enzyme that plays an important role in the intracellular glycolytic metabolic pathway and has been reported to promote tumor cell proliferation and invasion (47). To confirm the role of *ALDOA* in regulating cell proliferation in melanoma cells with *BRAF* mutation, cell proliferation was measured in A375 (BRAF V600E) and MEWO (triple-WT) melanoma cells with *ALDOA* silencing using the CCK-8 (Cell Counting Kit-8) assay. We found that cell proliferation was inhibited in melanoma cells with *ALDOA* silencing (**Fig. 6F**; Supplementary Fig. S10E–S10G).

Given the fact that it lacks therapy target of the triple-WT melanoma, we investigated gene expression profiles in the triple-WT melanomas and found that the expression of MET and glycoprotein *PTGDS* was specifically upregulated (**Fig. 6E**). The *PTGDS* is a member of the lipid transport protein superfamily and functions in regulating tumor cell proliferation (48). To identify the role of *PTGDS* in regulating the proliferation in triple-WT melanoma, we silenced the *PTGDS* gene by small interfering RNA in a triple-WT melanoma cell line, MEWO. We found that the cellular proliferation was inhibited in MEWO cells with *PTGDS* silencing (**Fig. 6F**; Supplementary Fig. S10C–S10G; ref. 49). To further identify the role of *PTGDS* in regulating tumor growth *in vivo*, the melanoma xenograft model was used. We found that *PTGDS* silencing significantly inhibited tumor growth *in vivo* (**Fig. 6G** and **H**). These results indicate that *PTGDS* is a potential therapeutic target of the triple-WT melanoma.

The molecular classifications of AM and MM based on the single-cell transcriptome

Molecular classification is able to guide the targeted treatment of melanoma (16). To uncover the more precise molecular classification of melanoma, we performed a NMF analysis based on the unique biological characteristics of scRNA-seq of melanoma. Overall, we identified both common and specific molecular MPs of each melanoma subtype. The MP of cell cycle (*MKI67*/*TOP2A*/*UBE2C*) is the common feature in all types of melanoma. The activation of ATP metabolism (*JUN*/*IER2*/*FOS*) was specifically found in AM (**Fig. 7A**; Supplementary Table S5). Similarly, CM presented with a unique MP associated with a transporter activity (*LRRC23*/*SLC2A14*/*STPG4*; **Fig. 7B**; Supplementary Table S5). Notably, the MP of antigen presentation is specifically identified in MM. This program is characterized by pathways involved in antigen processing, peptide presentation, and MHC molecules. The pathways of immune response are mediated by *FCER1G*/*HLA-DRA*/*HSPA6* signaling (**Fig. 7C**; Supplementary Table S5). To strengthen the reliability of our findings and mitigate the constraint of having a limited number

of CM samples, we used single-cell transcriptome data from 23 untreated patients with CM, obtained from a publicly available database, to conduct NMF analysis. We found that the most prominent feature of CM remains high replication (MP2), which is consistent with the results we obtained from the analysis of the three CM cases (Supplementary Fig. S11A and S11B).

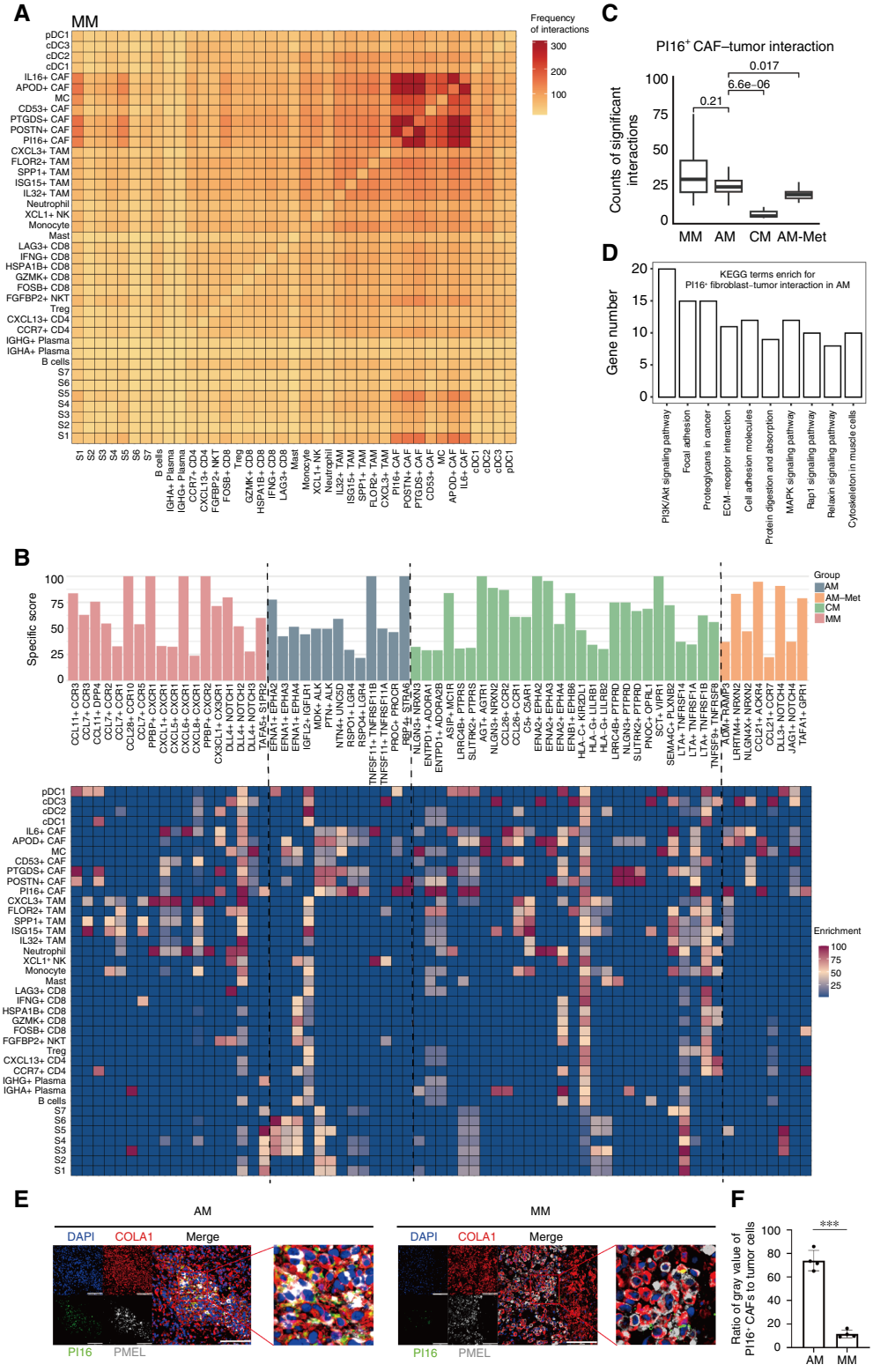

To further explore whether the specific MP of antigen presentation in MM is clinically associated with the treatment response of immunotherapy, a total of five patients with MM underwent treatment of surgical resection and postoperative immunotherapy. Specifically, we scored each patient based on the two MPs in the molecular classification of MM (Supplementary Table S5). Patients with low activity of the antigen-presentation (MP1) program and high activity of the proliferation (MP2) program were deemed as high risk. By contrast, other combinations of MP1 and MP2 were considered as low risk. Surprisingly, after approximately 12 months of clinical follow-up, two patients who were classified as high risk experienced recurrence, whereas all three patients who were recognized as low risk showed no evidence of disease recurrence (**Fig. 7D**). Higher MP1 scores and lower MP2 scores showed trends of better prognosis (**Fig. 7E**). Moreover, KM analysis revealed that patients in the high-risk group were significantly associated with poorer prognosis (**Fig. 7F**; Supplementary Fig. S11C; Supplementary Table S6). Our classification approach therefore demonstrates a promising potential in guiding clinical treatment. Patients with MM with negative MP1 scores and positive MP2 scores exhibit poorer responses to immunotherapy.

To enhance the robustness of our conclusions and compensate for the limited number of CM samples, we used single-cell transcriptome data from 23 untreated patients with CM sourced from a public database for reanalysis. We found that the proportion of the S5 tumor cell subpopulation in CM was significantly lower than it was in MM, which is fully consistent with our previous findings (Supplementary Fig. S12A–S12C). Furthermore, the level of exhausted $LAG3^+$ $CD8^+$ T cells in CM was significantly higher than it was in AM and MM (Supplementary Fig. S12D and S12E), aligning with the increased sensitivity of CM to anti–PD-1 therapy (50). Additionally, the proportions of neutrophils and $CXCL3^+$ TAMs within the myeloid cell population were higher in MM than in AM and CM, including the 23 CM cases from the public database (Supplementary Fig. S12F–S12G). Although the proportion of $PI16^+$ CAFs varied when more CM samples were included in the analysis (Supplementary Fig. S12H and S12I), our focus was on the effect of $PI16^+$ CAFs on tumor cells; thus this did not affect our conclusions about CAFs. Overall, our conclusions are sufficiently reliable as validated by the public database.

Discussion

MM and AM are characterized with less mutation burden and expression of tumor antigens when compared with CM. Thus, both are usually not sensitive to the current available targeted therapy and immunotherapy in comparison with nonacral CM (50). Patients with MM and AM are usually diagnosed at late stages with remote metastases. Given the fact that there are very few reports on the transcriptomic landscape of MM, in this study, we compared the single-cell transcriptomic and genomic landscapes of 42 melanomas of different anatomical locations, including 11 MMs and 28 AMs. The results revealed that tumor cells exhibit common yet diverse composition and evolutionary routes in MM and AM that we also were able to show contained specific types of stromal and immune cells. Moreover, the antigen presentation type and the cell cycle activation type of MM identified in this study were found to possess promising potential in guiding clinical treatment.

MM, which originates from melanocytes in the respiratory, gastrointestinal, and urogenital tract, is an aggressive subtype of melanoma that is rare in Caucasians and accounts for 0.8% to 3.7% of all melanomas (51–53). The molecular basis for the aggressive phenotype in MM remains unknown. Herein, we identified that MM had an abundant S5 subgroup in which there was a high level of *MGP* and *PCOLCE* expression and which was specifically enriched with the expression of genes associated with EMT. Furthermore, specific types of immune cells, including neutrophils and $CXCL3^+$ tumor-associated macrophages were identified in MM. Both immune cells are immunosuppressive. Additionally, the strongest LR interactions among melanoma cells and stromal cells were observed in MM. Together, these characteristics of MM may explain why MM is more aggressive than CM. The stromal immunity features of MM are also consistent with the immunotherapy response rate of MM, which is higher than it is for AM and less than it is in CM (50).

Recent research on the immune features of AM has illustrated a generally impaired immune landscape, characterized by a low infiltration of T cells and NK cells and a high infiltration of Tregs (12, 14). However, with a significantly larger sample size, our analysis revealed that none of the proportions of distinct $CD4^+$ T, $CD8^+$ T, Treg, and NK cells in AM and CM reached statistical significance. Moreover, when examining the functions of these T cells, our analysis further revealed that T cells in AM exhibited the lowest exhaustion score, whereas those in CM demonstrated the highest exhaustion score. These results challenge the prevalent view that the ineffectiveness of immunotherapy for AM when compared with CM is due to the lack of immune infiltration or immune exhaustion (14). Our results indicate that the lowest cytotoxic score of T cells was characterized in AM. Furthermore, the high *TIGIT* expression in Tregs was found in AM. In addition, the lower expression of PDCD1 and CTLA4 in Tregs of AM might also contribute to the ineffectiveness of immunotherapy. Our analysis highlights the potential effectiveness of immunotherapy targeting *TIGIT* for AM. Although a recent study mentioned higher *TIGIT* in AM as a potential target of immunotherapy, they did not reach statistical significance because of the limited sample size (14). Besides, aside from the distinct immune features of AM compared with other melanoma subtypes, our study further compared the distinct immune characteristics between AM and AM-Met. In contrast to the nonsignificant proportions of immune cells in most melanoma subtypes, our study revealed significantly lower Treg levels in AM-Met than in AM. This was accompanied by a lower expression of immune checkpoints such as *CTLA4* and *TIGIT* in Treg, which further explains the highest cytotoxic score of T cells in AM-Met compared with other melanoma subtypes. This contrast in immune features

Figure 5.

Strong interactions among melanoma cells and stromal cells were observed in MM. **A,** Heatmaps of cell–cell interaction in MM. **B,** Bar plot (top) showing subtype-specific LR pairs in MM, AM, AM-Met, and CM, and heatmap (bottom) showing the enrichment of these LR pairs in cell clusters. **C,** Boxplot of cell–cell interaction between $PI16^+$ fibroblasts and melanoma cells. *P* values were calculated using the Wilcoxon rank-sum test. **D,** Kyoto Encyclopedia of Genes and Genomes (KEGG) enriched functional terms of the genes mediating interactions between $PI16^+$ fibroblasts and melanoma cells. ECM, extracellular matrix. **E** and **F,** IF staining indicating co-localization (**E**) and quantification ratio (**F**) of $PI16^+$ fibroblasts and melanoma cells in AM and MM. Cells were stained with anti-COLA1 (red), anti-PI16 (green), anti-PMEL (white), and DAPI (4',6-diamidino-2-phenylindole; blue). Quantification was based on a representative field of view. Scale bar, 100 μm. $P = 0.00028$.

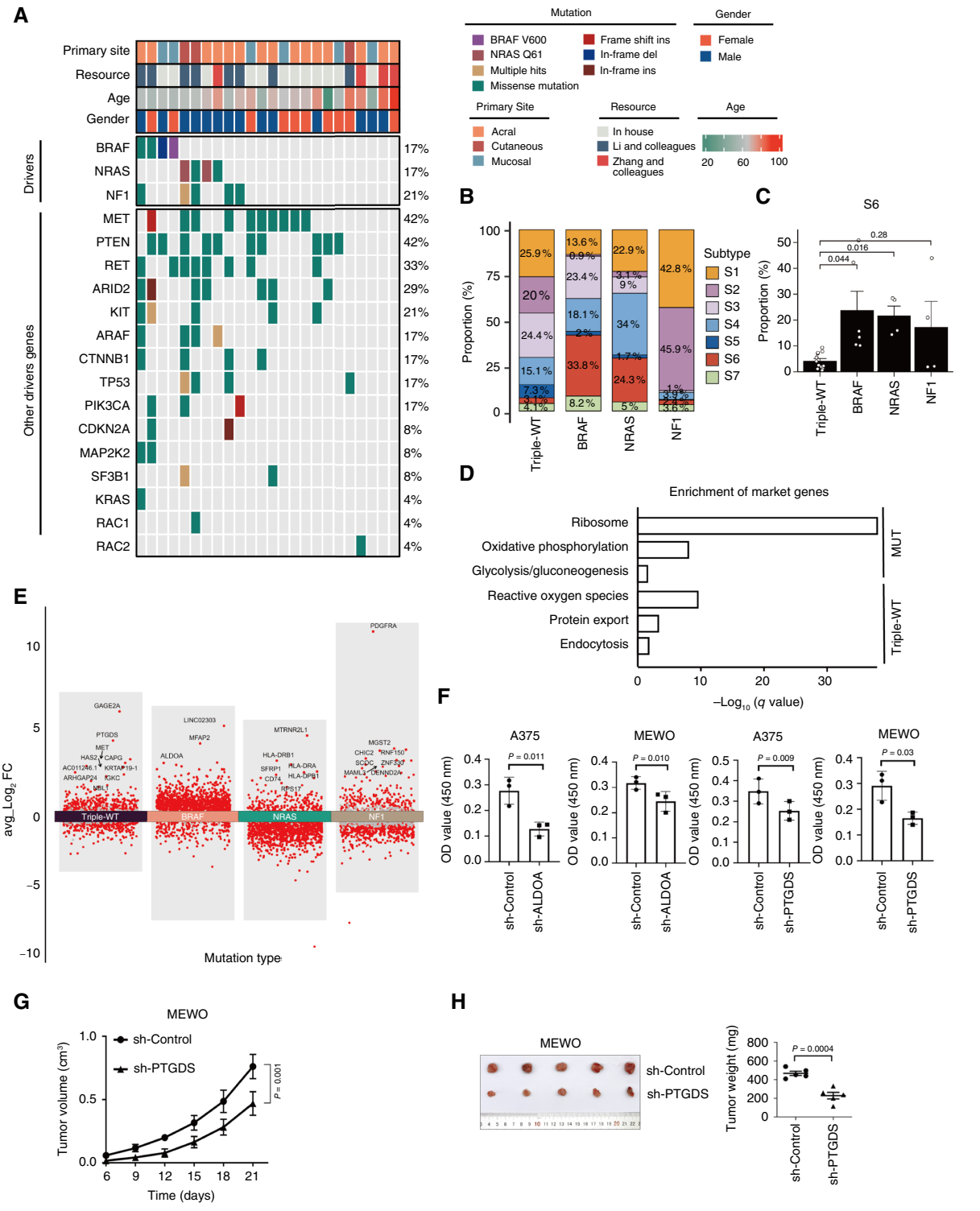

Figure 6.

Stem-like subtype cells; S6 of melanoma plays an important role in melanoma with driver mutant. **A,** Landscape of somatic alterations. **B,** Bar plot displaying the population distribution of seven melanoma subtypes within the triple-WT, BRAF, NRAS, and NF1 mutation groups. **C,** Histogram illustrating the populations of S6 subtype in AM, AM-Met, CM, and MM groups. The two-sided unpaired Student *t* test was used to identify the significant difference. Error bars represent mean ± SEM. **D,** Enriched functional terms of mutation and triple-WT. **E,** Volcano plot indicating differentially expressed genes (DEG) of S6 in the annotated mutation cells. **F,** CCK-8 trial after knocking down the DEGs. The bar plot shows the OD (optical density) value of the CKK-8 trial. **G** and **H,** Growth curve (**G**), tumor weight (**H**), and dissected tumors (**H**) for the xenograft experiments with indicated cells inoculated subcutaneously into the flanks of nude mice. Visible tumors were measured every 3 days. Data are mean ± SEM relative to the control group ($n = 5$).

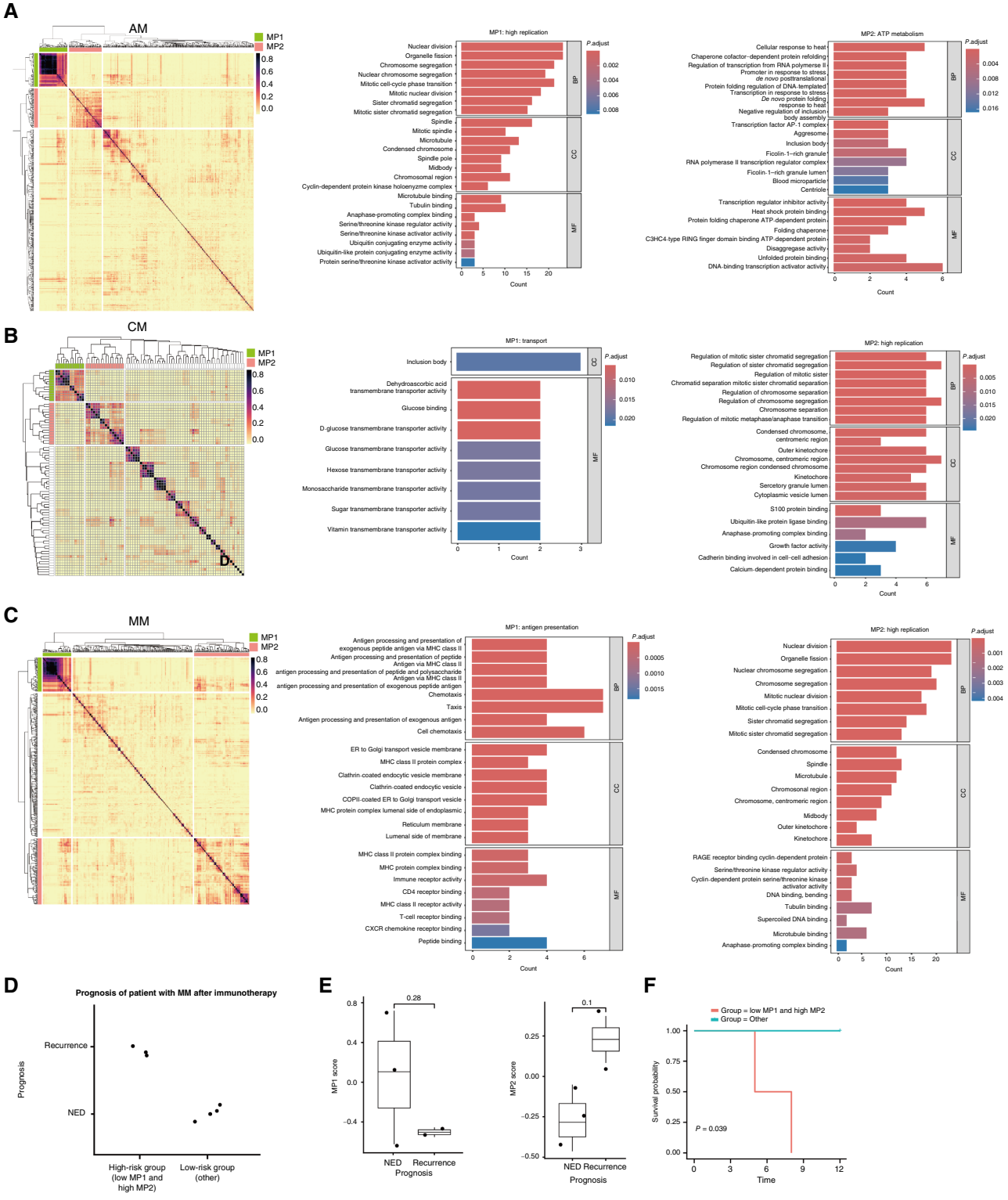

Figure 7.

Distinct molecular classifications of MM. **A,** Heatmaps of NMF analysis in AM. Bar plots displaying the representative Gene Ontology (GO) pathway terms enriched in each NMF MP. **B,** Heatmaps of NMF analysis in CM. Bar plots displaying the representative GO pathway terms enriched in each NMF MP. **C,** Heatmaps of NMF analysis in MM. Bar plots displaying the representative GO pathway terms enriched in each NMF MP. **D,** Patients with MM based on MP1 and MP2 scores, as well as no evidence of disease (NED) and recurrence. **E,** Boxplots illustrating the MP1 score of NED and recurrence group. **F,** KM analysis (right) showing the overall survival rate of patients with MM with the high-risk group (low MP1 score and high MP2 score) and the low-risk group (other) using the two-sided log-rank test. BP, biological process; CC, cell component; MF, molecular function; P.adjust, *P* value adjusted.

between AM and AM-Met suggests the need for completely different treatment strategies for patients with AM after metastasis. Finally, despite the detailed investigation into the immune landscape of AM, the characteristics of stromal cells in AM have not been well characterized. Although a recent study defined a new cluster of CAFs in AM. However, no evidence showed that this new cluster of CAFs was any different from that found in other melanoma subtypes (54). In this study, we showed that PI16$^+$ CAFs are significantly more prevalent in AM than in CM and MM. Importantly, these CAFs exhibit significantly higher levels of interaction with tumor cells through a series of AM-specific LR pairs, likely activating *PI3K*/*AKT* signaling and contributing to the malignancy. *PI16* is a marker of fibroblasts with stem-like features (45). Scarce but controversial features about PI16$^+$ CAF have been revealed (55, 56). Its specificity and frequent interaction with tumor cells in AM help illustrate the novel roles of these cells within tumor microenvironments.

The frequent mutational activation of *BRAF* was identified in CM in 2002 (57). A substantial effort has been made to identify additional driver mutations in melanoma since then. The analysis of large-scale melanoma exosome data of 135 CMs displayed five novel melanoma genes, namely, *RAC1*, *SNX31*, *TACC1*, *STK19*, and *ARID2* (58), with new therapeutics that target *RAC1*, *STK19*, or *ARID2* being developed and evaluated (59–62). The genomic landscape of AM and MM are very different with nonacral CM. AM frequently harbors mutations in Ras family members *NRAS*, *KRAS*, and *HRAS* (accounting for 22%), *KIT* (15%), *BRAF* (8%), and *TP53* (4%; refs. 63, 64). Similarly, MM also carries *BRAF* and *NRAS* mutations, albeit at lower frequencies than CM. Instead, *KIT* mutations, as well as *TERT* promoter mutations, *CCND1* amplifications, and *CDK4* amplifications, are more prevalent in AM and MM, playing critical roles in promoting cell proliferation and evading apoptosis (4, 65). One most recent study indicates that AM *in situ* tumors with invasive features exhibit more clonal mutations and poorer genomic stability (16). However, there are few studies that have examined the single-cell transcriptomic landscape in melanoma with specific driver mutations, especially in AM and MM. In this study, we paired 21 cases of WES with scRNA-seq and linked driver mutations with specific transcriptomic landscape. Melanoma with *BRAF* and *NRAS* mutations were characterized by cells with a high expression of ALDOA$^+$ and GLMP$^+$, which serve as the common ancestor of other melanoma cells (**Fig. 6**). Most of MMs originated from MGP$^+$ and IGFBP$^+$ cells. These cells are characterized by high EMT potential and are prominent through all phases (**Fig. 1**). This linkage indicates the specific role of specific driver mutations in melanoma development.

Melanoma is a highly heterogeneous skin cancer characterized by diverse genetic, cellular, and microenvironmental factors. Molecular typing is crucial for its diagnosis and treatment. Genetic testing was recommended for all patients with melanoma to identify some key molecular targets including *BRAF*, *KIT*, and *NRAS* (66). Based on the occurrence of driver mutations only, melanoma was classified into four genomic subtypes, including *BRAF* mutation, *NRAS* mutation, *NF1* loss, and triple-WT (32). These subtypes do not correlate with histopathological features and the site of origin. Most AMs and MMs fall into the triple-WT subtype (10). One recent report clustered 81 AM samples with bulk RNA-seq data and identified three distinct molecular subtypes, including the "keratin" subtype C1, "chromatin remodeling" subtype C2, and "proliferation" subtype C3 (16). In this study, our classification based on single-cell transcriptome confirmed the "proliferation" subtype of AM and found a "high-metabolism" subtype of AM (**Fig. 7A**). The "proliferation" subtype was also identified in MM. Another subtype identified in MM was an antigen presentation subtype, which revealed a promising potential in guiding clinical treatment of MM (**Fig. 7E** and **F**). Although it cannot be used to guide treatment as therapies targeting specific driver mutations, the classification of AA and MM on the basis of bulk RNA and single-cell transcriptome should be helpful in guiding combination treatment strategies of melanoma.

Authors' Disclosures

No disclosures were reported.

Authors' Contributions

Y. Li: Conceptualization, resources, data curation, software, formal analysis, methodology, writing–original draft, writing–review and editing. **Z. Cui:** Software, formal analysis, methodology, writing–review and editing. **X. Song:** Resources, formal analysis, methodology. **Y. Chen:** Formal analysis, methodology, writing–review and editing. **Cang Li:** Data curation, supervision, methodology, writing–original draft, writing–review and editing. **J. Shi:** Formal analysis, methodology. **W. Qian:** Resources, formal analysis. **G. Ren:** Resources. **J. Zhou:** Formal analysis. **Chunpu Li:** Formal analysis. **X. Ma:** Formal analysis. **Y. Chen:** Formal analysis. **D. Jia:** Resources, formal analysis. **Y. Zhang:** Formal analysis, methodology. **Zhilin Zhang:** Formal analysis. **R. Zhang:** Formal analysis. **Zhaotian Zhang:** Formal analysis. **Y. Chen:** Resources. **Z. Xu:** Supervision. **W. Chen:** Resources, supervision. **X. Miao:** Supervision. **H. Yu:** Resources, supervision. **J. Chen:** Supervision, methodology. **K. Wang:** Supervision. **C.R. Goding:** Supervision, writing–review and editing. **Z. Wei:** Supervision, methodology, writing–review and editing. **T. Li:** Resources, supervision. **R. Cui:** Conceptualization, supervision, funding acquisition, methodology.

Acknowledgments

This work was supported by the National Key Research and Development Program of China (grant numbers 2021YFA1101000 and 2021YFA1101004), the National Natural Science Foundation of China (grant number U21A20379), the Research Fund for Foreign Scholars of China (grant number 82250710176), and the leading innovation and entrepreneurship team of Hangzhou (TD2020006).

Note

Supplementary data for this article are available at Clinical Cancer Research Online (http://clincancerres.aacrjournals.org/).

Received September 24, 2024; revised November 29, 2024; accepted April 3, 2025; posted first April 7, 2025.

References

1. de Visser KE, Joyce JA. The evolving tumor microenvironment: from cancer initiation to metastatic outgrowth. Cancer Cell 2023;41:374–403.
2. Kalaora S, Nagler A, Wargo JA, Samuels Y. Mechanisms of immune activation and regulation: lessons from melanoma. Nat Rev Cancer 2022;22:195–207.
3. Bald T, Quast T, Landsberg J, Rogava M, Glodde N, Lopez-Ramos D, et al. Ultraviolet-radiation-induced inflammation promotes angiotropism and metastasis in melanoma. Nature 2014;507:109–13.
4. Newell F, Johansson PA, Wilmott JS, Nones K, Lakis V, Pritchard AL, et al. Comparative genomics provides etiologic and biological insight into melanoma subtypes. Cancer Discov 2022;12:2856–79.
5. Lian B, Cui CL, Zhou L, Song X, Zhang XS, Wu D, et al. The natural history and patterns of metastases from mucosal melanoma: an analysis of 706 prospectively-followed patients. Ann Oncol 2017;28:868–73.
6. Mihajlovic M, Vlajkovic S, Jovanovic P, Stefanovic V. Primary mucosal melanomas: a comprehensive review. Int J Clin Exp Pathol 2012;5:739–53.

7. Nassar KW, Tan AC. The mutational landscape of mucosal melanoma. Semin Cancer Biol 2020;61:139–48.
8. Curtin JA, Fridlyand J, Kageshita T, Patel HN, Busam KJ, Kutzner H, et al. Distinct sets of genetic alterations in melanoma. N Engl J Med 2005;353:2135–47.
9. Bai X, Mao LL, Chi ZH, Sheng XN, Cui CL, Kong Y, et al. BRAF inhibitors: efficacious and tolerable in BRAF-mutant acral and mucosal melanoma. Neoplasma 2017;64:626–32.
10. Wang M, Banik I, Shain AH, Yeh I, Bastian BC. Integrated genomic analyses of acral and mucosal melanomas nominate novel driver genes. Genome Med 2022;14:65.
11. Jung S, Johnson DB. Management of acral and mucosal melanoma: medical oncology perspective. Oncologist 2022;27:703–10.
12. Zhang C, Shen H, Yang T, Li T, Liu X, Wang J, et al. A single-cell analysis reveals tumor heterogeneity and immune environment of acral melanoma. Nat Commun 2022;13:7250.
13. Wei C, Sun W, Shen K, Zhong J, Liu W, Gao Z, et al. Delineating the early dissemination mechanisms of acral melanoma by integrating single-cell and spatial transcriptomic analyses. Nat Commun 2023;14:8119.
14. Li J, Smalley I, Chen Z, Wu JY, Phadke MS, Teer JK, et al. Single-cell characterization of the cellular landscape of acral melanoma identifies novel targets for immunotherapy. Clin Cancer Res 2022;28:2131–46.
15. He Z, Xin Z, Yang Q, Wang C, Li M, Rao W, et al. Mapping the single-cell landscape of acral melanoma and analysis of the molecular regulatory network of the tumor microenvironments. Elife 2022;11:e78616.
16. Liu H, Gao J, Feng M, Cheng J, Tang Y, Cao Q, et al. Integrative molecular and spatial analysis reveals evolutionary dynamics and tumor-immune interplay of in situ and invasive acral melanoma. Cancer Cell 2024;42:1067–85.e11.
17. Pozniak J, Pedri D, Landeloos E, Van Herck Y, Antoranz A, Vanwynsberghe L, et al. A TCF4-dependent gene regulatory network confers resistance to immunotherapy in melanoma. Cell 2024;187:166–83.e25.
18. Butler A, Hoffman P, Smibert P, Papalexi E, Satija R. Integrating single-cell transcriptomic data across different conditions, technologies, and species. Nat Biotechnol 2018;36:411–20.
19. Korsunsky I, Millard N, Fan J, Slowikowski K, Zhang F, Wei K, et al. Fast, sensitive and accurate integration of single-cell data with Harmony. Nat Methods 2019;16:1289–96.
20. Chen S, Zhou Y, Chen Y, Gu J. fastp: an ultra-fast all-in-one FASTQ preprocessor. Bioinformatics 2018;34:i884–90.
21. Li H, Durbin R. Fast and accurate short read alignment with Burrows-Wheeler transform. Bioinformatics 2009;25:1754–60.
22. McLaren W, Gil L, Hunt SE, Riat HS, Ritchie GR, Thormann A, et al. The ensembl variant effect predictor. Genome Biol 2016;17:122.
23. Tian T, Zhang J, Lin X, Wei Z, Hakonarson H. Model-based deep embedding for constrained clustering analysis of single cell RNA-seq data. Nat Commun 2021;12:1873.
24. Hafemeister C, Satija R. Normalization and variance stabilization of single-cell RNA-seq data using regularized negative binomial regression. Genome Biol 2019;20:296.
25. Aibar S, González-Blas CB, Moerman T, Huynh-Thu VA, Imrichova H, Hulselmans G, et al. SCENIC: single-cell regulatory network inference and clustering. Nat Methods 2017;14:1083–6.
26. Azizi E, Carr AJ, Plitas G, Cornish AE, Konopacki C, Prabhakaran S, et al. Single-cell map of diverse immune phenotypes in the breast tumor microenvironment. Cell 2018;174:1293–308.e36.
27. Qiu X, Hill A, Packer J, Lin D, Ma YA, Trapnell C. Single-cell mRNA quantification and differential analysis with Census. Nat Methods 2017;14:309–15.
28. Cao J, Spielmann M, Qiu X, Huang X, Ibrahim DM, Hill AJ, et al. The single-cell transcriptional landscape of mammalian organogenesis. Nature 2019;566:496–502.
29. Hänzelmann S, Castelo R, Guinney J. GSVA: gene set variation analysis for microarray and RNA-seq data. BMC Bioinformatics 2013;14:7.
30. Efremova M, Vento-Tormo M, Teichmann SA, Vento-Tormo R. CellPhoneDB: inferring cell-cell communication from combined expression of multi-subunit ligand-receptor complexes. Nat Protoc 2020;15:1484–506.
31. Jin S, Guerrero-Juarez CF, Zhang L, Chang I, Ramos R, Kuan CH, et al. Inference and analysis of cell-cell communication using CellChat. Nat Commun 2021;12:1088.
32. Akbani R, Akdemir K, Aksoy B, Albert M, Ally A, Amin S, et al. Genomic classification of cutaneous melanoma. Cell 2015;161:1681–96.
33. Robinson MD, McCarthy DJ, Smyth GK. edgeR: a Bioconductor package for differential expression analysis of digital gene expression data. Bioinformatics 2010;26:139–40.
34. Tirosh I, Izar B, Prakadan SM, Wadsworth MH, Treacy D, Trombetta JJ, et al. Dissecting the multicellular ecosystem of metastatic melanoma by single-cell RNA-seq. Science 2016;352:189–96.
35. Cavallaro U, Schaffhauser B, Christofori G. Cadherins and the tumour progression: is it all in a switch? Cancer Lett 2002;176:123–8.
36. Zheng L, Qin S, Si W, Wang A, Xing B, Gao R, et al. Pan-cancer single-cell landscape of tumor-infiltrating T cells. Science 2021;374:abe6474.
37. Klemen ND, Wang M, Rubinstein JC, Olino K, Clune J, Ariyan S, et al. Survival after checkpoint inhibitors for metastatic acral, mucosal and uveal melanoma. J Immunother Cancer 2020;8:e000341.
38. Johnston RJ, Comps-Agrar L, Hackney J, Yu X, Huseni M, Yang Y, et al. The immunoreceptor TIGIT regulates antitumor and antiviral CD8(+) T cell effector function. Cancer Cell 2014;26:923–37.
39. Sun K, Xu R, Ma F, Yang N, Li Y, Sun X, et al. scRNA-seq of gastric tumor shows complex intercellular interaction with an alternative T cell exhaustion trajectory. Nat Commun 2022;13:4943.
40. Shoushtari AN, Munhoz RR, Kuk D, Ott PA, Johnson DB, Tsai KK, et al. The efficacy of anti-PD-1 agents in acral and mucosal melanoma. Cancer 2016;122:3354–62.
41. Cheng S, Li Z, Gao R, Xing B, Gao Y, Yang Y, et al. A pan-cancer single-cell transcriptional atlas of tumor infiltrating myeloid cells. Cell 2021;184:792–809.e23.
42. Gullotta GS, De Feo D, Friebel E, Semerano A, Scotti GM, Bergamaschi A, et al. Age-induced alterations of granulopoiesis generate atypical neutrophils that aggravate stroke pathology. Nat Immunol 2023;24:925–40.
43. Yu X, Li C, Wang Z, Xu Y, Shao S, Shao F, et al. Neutrophils in cancer: dual roles through intercellular interactions. Oncogene 2024;43:1163–77.
44. Cords L, Tietscher S, Anzeneder T, Langwieder C, Rees M, de Souza N, et al. Cancer-associated fibroblast classification in single-cell and spatial proteomics data. Nat Commun 2023;14:4294.
45. Buechler MB, Pradhan RN, Krishnamurty AT, Cox C, Calviello AK, Wang AW, et al. Cross-tissue organization of the fibroblast lineage. Nature 2021;593:575–9.
46. Biffi G, Tuveson DA. Diversity and biology of cancer-associated fibroblasts. Physiol Rev 2021;101:147–76.
47. Song J, Li H, Liu Y, Li X, Shi Q, Lei QY, et al. Aldolase A accelerates cancer progression by modulating mRNA translation and protein biosynthesis via noncanonical mechanisms. Adv Sci (Weinh) 2023;10:e2302425.
48. Wu W, Li H, Wang Z, Dai Z, Liang X, Luo P, et al. The tertiary lymphoid structure-related signature identified PTGDS in regulating PD-L1 and promoting the proliferation and migration of glioblastoma. Heliyon 2024;10:e23915.
49. Ercolano G, De Cicco P, Rubino V, Terrazzano G, Ruggiero G, Carriero R, et al. Knockdown of PTGS2 by CRISPR/CAS9 system designates a new potential gene target for melanoma treatment. Front Pharmacol 2019;10:1456.
50. Ascierto PA, Del Vecchio M, Mandalá M, Gogas H, Arance AM, Dalle S, et al. Adjuvant nivolumab versus ipilimumab in resected stage IIIB-C and stage IV melanoma (CheckMate 238): 4-year results from a multicentre, double-blind, randomised, controlled, phase 3 trial. Lancet Oncol 2020;21:1465–77.
51. McLaughlin CC, Wu XC, Jemal A, Martin HJ, Roche LM, Chen VW. Incidence of noncutaneous melanomas in the U.S. Cancer 2005;103:1000–7.
52. Goldemberg DC, Thuler LCS, de Melo AC. An update on mucosal melanoma: future directions. Acta Dermatovenerol Croat 2019;27:11–5.
53. Chang AE, Karnell LH, Menck HR. The national cancer data base report on cutaneous and noncutaneous melanoma: a summary of 84,836 cases from the past decade. The American College of Surgeons Commission on cancer and the American Cancer Society. Cancer 1998;83:1664–78.
54. Wang P, Ma Y, Zhao Y, Li Y, Tang C, Wang S, et al. Single-cell RNA sequencing unveils tumor heterogeneity and immune microenvironment between subungual and plantar melanoma. Sci Rep 2024;14:7039.
55. Krishnamurty AT, Shyer JA, Thai M, Gandham V, Buechler MB, Yang YA, et al. LRRC15^{+} myofibroblasts dictate the stromal setpoint to suppress tumour immunity. Nature 2022;611:148–54.
56. Elyada E, Bolisetty M, Laise P, Flynn WF, Courtois ET, Burkhart RA, et al. Cross-species single-cell analysis of pancreatic ductal adenocarcinoma reveals antigen-presenting cancer-associated fibroblasts. Cancer Discov 2019;9:1102–23.
57. Davies H, Bignell GR, Cox C, Stephens P, Edkins S, Clegg S, et al. Mutations of the BRAF gene in human cancer. Nature 2002;417:949–54.
58. Schadendorf D, Fisher DE, Garbe C, Gershenwald JE, Grob JJ, Halpern A, et al. Melanoma. Nat Rev Dis Primers 2015;1:15003.
59. Hodis E, Watson IR, Kryukov GV, Arold ST, Imielinski M, Theurillat JP, et al. A landscape of driver mutations in melanoma. Cell 2012;150:251–63.

60. Cannon AC, Budagyan K, Uribe-Alvarez C, Kurimchak AM, Araiza-Olivera D, Cai KQ, et al. Unique vulnerability of RAC1-mutant melanoma to combined inhibition of CDK9 and immune checkpoints. Oncogene 2024;43:729–43.
61. Yin C, Zhu B, Zhang T, Liu T, Chen S, Liu Y, et al. Pharmacological targeting of STK19 inhibits oncogenic NRAS-driven melanomagenesis. Cell 2019;176: 1113–27.e16.
62. Moreno T, Monterde B, González-Silva L, Betancor-Fernández I, Revilla C, Agraz-Doblas A, et al. ARID2 deficiency promotes tumor progression and is associated with higher sensitivity to chemotherapy in lung cancer. Oncogene 2021;40:2923–35.
63. Farshidfar F, Rhrissorrakrai K, Levovitz C, Peng C, Knight J, Bacchiocchi A, et al. Integrative molecular and clinical profiling of acral melanoma links focal amplification of 22q11.21 to metastasis. Nat Commun 2022;13: 898.
64. Shi Q, Liu L, Chen J, Zhang W, Guo W, Wang X, et al. Integrative genomic profiling uncovers therapeutic targets of acral melanoma in asian populations. Clin Cancer Res 2022;28:2690–703.
65. Hintzsche JD, Gorden NT, Amato CM, Kim J, Wuensch KE, Robinson SE, et al. Whole-exome sequencing identifies recurrent SF3B1 R625 mutation and comutation of NF1 and KIT in mucosal melanoma. Melanoma Res 2017;27: 189–99.
66. Chinese Society of Pathology Dermatopathology Group of Chinese Society of Pathology. [Chinese guidelines on standardized pathological diagnosis of melanoma (2021 version)]. Zhonghua Bing Li Xue Za Zhi 2021;50:572–82.